Nonlinear Control Methods for Reluctance Actuator with Hysteresis

January 2015

LIU YU-PING

Graduate School of Engineering

CHIBA UNIVERSITY

(千葉大学審査学位論文)

Nonlinear Control Methods for Reluctance Actuator with Hysteresis

January 2015

LIU YU-PING

Graduate School of Engineering

CHIBA UNIVERSITY

Abstract

The next-generation semiconductor lithography equipment needs a suitable actuator to meet the requirement of high-acceleration, high-speed and high-precision. Reluctance linear actuator, which has a unique property of small volume, low current and high power density, is a very suitable candidate. One of the major challenges in the application of reluctance actuator is the hysteresis of the force, which has a strong nonlinearity about the current and is directly related to the final accuracy in the nanometer range. Therefore, it is necessary to study the control method for the hysteresis in reluctance force. The main contributions of this thesis are as follows:

1. The reluctance actuator models without hysteresis for C-core and E-core reluctance linear actuator are reviewed and then the reluctance actuator models with hysteresis are proposed.
2. A hysteresis current compensation configuration for the reluctance actuator with hysteresis based on the adaptive multi-layer neural network, which is used as a learning machine of hysteresis, is proposed. The main contributions of this method is a hysteresis compensator for current-driven reluctance linear actuator using the adaptive MNN proposed for the first time and the inverse hysteresis model is not used.
3. A new nonlinear control method is proposed for the stage having paired reluctance linear actuator with hysteresis using the direct adaptive neural network. The feature of this method lies in that the nonlinear compensator in conventional methods, which computes the current reference from that of the input and output

force, is not used. This naturally overcomes the robustness issue with respect to parameter uncertainty.

4. An acceleration feedback is designed for the fine stage having paired reluctance linear actuator with hysteresis. The feature of this method lies in that by considering the hysteresis force as a disturbance force, an acceleration feedback loop i s designed to reduce the influence of the hysteresis force. The proposed method can improve the process sensitivity for low frequencies and remove the high-bandwidth requirement. Acceleration feedback implementation in digital controller and the control for a fine stage connected to a coarse stage are discussed.

Simulation results show that the proposed methods are effective in overcoming the hysteresis and promising in high-precision and high acceleration control applications.

To my parents
my wife
my sons

Acknowledgements

I would like to express my sincerest gratitude to my adviser, Prof. Kang-Zhi Liu, for his guidance and support in the process of completing this work. His serious attitudes towards scientific research have been a model for me and many other things that I learned from him will be of great help to me during my career.

I would like to express my deep thanks to Prof. Xiaofeng Yang for giving me the opportunity of the project and the suggestions during the research process.

I am also grateful to the students Wei Wang, Ya Wei, Yinghui Wang, Kai Ye and Zhenhai Pan. I cannot forget their unselfish help to me at the beginning of the oversea study.

Finally, I would like to thank my wife Xiaolin Ye for her generous support, understanding, patience and endless love. Without her consistent support, my doctor course would not have been completed. I also thank our parents for giving us unselfish love, which is the source of my studying.

Contents

List of Figures ix

List of Tables xiii

1 Introduction 1

1.1 Lithographic process in semiconductor manufacturing 1

1.2 Review of the lithographic tool 2

1.2.1 Stepper 2

1.2.2 Scanner 4

1.2.3 Dual-stage scanner 6

1.3 Challenge to the next-generation fine stage actuator 8

1.4 Reluctance linear actuator and hysteresis control 10

1.4.1 Reluctance linear actuator 10

1.4.2 Hysteresis compensation control based on the inverse hysteresis model 11

1.5 Research objectives 12

1.5.1 The main features 12

1.5.2 The main contributions 12

1.6 Thesis layout 13

2 Reluctance Linear Actuator Models with Hysteresis 15

2.1 Introduction 15

2.2 Hysteresis model 15

2.2.1 Review of the hysteresis model 15

2.2.2 Parametric hysteresis operator 16

2.2.3 H and B model using hysteresis operator 19
2.3 Models for reluctance linear actuator with C-core 20
2.3.1 Magnetism principle 20
2.3.2 Magnetic circuit 20
2.3.3 Flux density without hysteresis 21
2.3.4 Energy in the air gaps 22
2.3.5 Magnetic force without hysteresis 23
2.3.6 Flux density with hysteresis 24
2.3.7 Magnetic force with hysteresis 24
2.4 Models for reluctance linear actuator with E-core 25
2.4.1 Magnetic circuit 25
2.4.2 Flux density without hysteresis 27
2.4.3 Energy in the air gaps 31
2.4.4 Magnetic force without hysteresis 31
2.4.5 Flux density with hysteresis 32
2.4.6 Magnetic force with hysteresis 34
2.5 Conclusion 34

3 Nonlinear Control for Reluctance Linear Actuator 37
3.1 Introduction 37
3.2 Control of reluctance linear actuator 37
3.2.1 Nonlinear current compensation 37
3.2.2 Control of a stage having paired reluctance linear actuator 38
3.3 Conclusion 41

4 Hysteresis Compensation for a Current-driven Reluctance Linear Actuator Using Adaptive MNN 43
4.1 Introduction 43
4.2 Neural network 44
4.3 Design of nonlinear current compensator using adaptive MNN . . 46
4.4 Simulations 48
4.5 Conclusion 54

5 A Direct Adaptive MNN Control Method for Stage Having Paired Reluctance Linear Actuator with Hysteresis **57**
5.1 Introduction 57
5.2 Direct adaptive MNN control for reluctance linear actuator 58
5.2.1 Nonlinear control using adaptive neural network 58
5.2.2 Application to 1-DOF stage having paired reluctance linear actuator 59
5.3 Simulations 61
5.4 Conclusion 68

6 Acceleration Feedback in a Stage Having Paired Reluctance Linear Actuator with Hysteresis **69**
6.1 Introduction 69
6.2 Acceleration feedback control 70
6.2.1 Basic idea 70
6.2.2 Design of acceleration feedback in frequency domain 70
6.2.3 Acceleration feedback implementation for discretization . . 71
6.2.4 Acceleration feedback in a fine stage connected to a coarse stage 73
6.3 Simulations 74
6.4 Comparison of the proposed hysteresis compensation methods . . 79
6.5 Conclusion 82

7 Conclusions **83**

References **85**

List of Figures

1.1 Lithographic process 2
1.2 Current model stepper 3
1.3 Stepper layout 3
1.4 The main components of a wafer stepper 4
1.5 Current model scanner 5
1.6 Scanner layout 5
1.7 The step-and-scan principle in exposing a wafer 6
1.8 Current model dual-stage scanner 6
1.9 Dual-stage scanner layout 7
1.10 Historical cost of computer memory and storage 8
1.11 Voice actuator and reluctance actuator 9
1.12 C-core reluctance actuator 10
1.13 E-core reluctance actuator 10

2.1 Trajectories of the parametric hysteresis operator 17
2.2 Automata representation of the hysteresis operator 18
2.3 H and B curve 19
2.4 C-core I Magnetic circuit 21
2.5 E-core structure 25
2.6 E-core flux circuit 26
2.7 Simplified flux circuit 28
2.8 Curve of an input current and the corresponding output force . . 35

3.1 Typical current-driven reluctance actuator control loop 37
3.2 Paired E/I core actuator 39

LIST OF FIGURES

3.3 Basic control scheme 40
3.4 Paired E/I core actuator control 41

4.1 Structure of hysteresis current compensator 46
4.2 Reference force 49
4.3 Comparison of the force error 49
4.4 Comparison of the force hysteresis loop 51
4.5 Reference position and velocity 52
4.6 Comparison of the position tracking error 53
4.7 Position tracking error in the constant velocity segment 53
4.8 Position tracking error in the stop segment 54

5.1 Direct adaptive MNN control for reluctance linear actuator 58
5.2 Nonlinear control structure 60
5.3 Force command 62
5.4 Force error with nonlinear compensator 62
5.5 Force error with adaptive MNN controller 63
5.6 Comparison of the force hysteresis loop 64
5.7 Reference position and velocity 65
5.8 Comparison of the position tracking error 65
5.9 Outputs of the adaptive controllers 67
5.10 Output net force using the adaptive controller 67

6.1 Simplified virtual control scheme 71
6.2 Using $H_1(s)$ and $H_2(s)$ in the acceleration feedback loop 72
6.3 Discrete form of acceleration feedback 74
6.4 The final discrete form of acceleration feedback 74
6.5 Total feedback scheme 75
6.6 Reference position and velocity 77
6.7 Position tracking error 77
6.8 Position loop process sensitivity of the fine stage 78
6.9 Fine stage closed control loop bode plots 78
6.10 Coarse stage closed control loop bode plots 79
6.11 Comparison of the force following error 80

6.12 Reference position and velocity 81
6.13 Comparison of the position tracking error 82

LIST OF FIGURES

List of Tables

4.1 E/I parameters 48
4.2 E/I stage parameters 51
4.3 Trajectory values 52

5.1 E/I parameters 63
5.2 E/I stage parameters 66
5.3 Trajectory values 66

6.1 E/I parameters 75
6.2 E/I stage parameters 76

LIST OF TABLES

1

Introduction

In this chapter, the lithographic process in semiconductor manufacturing is introduced firstly; then we review the the historic development of the lithographic tool; after that, we discus the challenges in the next generation fine stage actuator; finally, we introduce the layout of this thesis.

1.1 Lithographic process in semiconductor manufacturing

In semiconductor manufacturing, the wafer is covered with a layer of photosensitive ink called resist . The optical system creates an image in the resist by the lithographic tool exposing a reticle pattern onto the wafer, The maximum size of one exposure area on the wafer, called a die, is typically 26×32 mm; one die can hold multiple separate IC images. Figure 1.1 shows a basic picture of the lithographic process [58]. The treated areas are determined by a resist layer, which contains a pattern that is previously imaged from the pattern on a mask by an optical exposure system.

Initially the exposure is done by direct illumination through a mask, which was closely positioned above the wafer. This shadow mask exposure principle is however limited in resolution by the laws of diffraction and suffers from vulnerability of the previous layers for damage by touching the surface of the mask [58]. To solve that issue, the wafer stepper and the wafer scanner were invented.

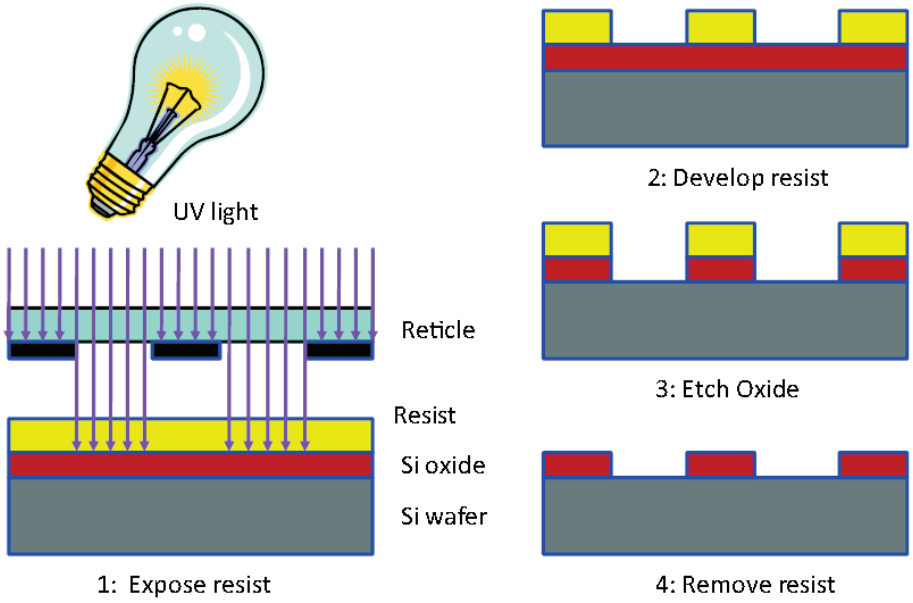

Figure 1.1: Lithographic process is a local chemical treatment of the silicon substrate (Courtesy of [58]).

1.2 Review of the lithographic tool

In the following, we will review the history of the lithographic equipment which is produced by the company ASML in the recent years [8].

1.2.1 Stepper

The stepper as shown in Figure 1.2 was the main lithographic tool used until about 1997. Figure 1.3 shows the stepper layout. The stepper exposes the complete wafer by stepping the wafer from one exposure location to the next. Light is switched off during the stepping motion. Each die on the wafer is exposed in a flash, after which the wafer is repositioned to the next die location. This process repeats itself until the full wafer is exposed [8].

Figure 1.4 shows the main components of a wafer stepper. The optical projection system is located in the center. Like a slide projector that projects light through a transparency and a lens to the wall, a wafer stepper projects light through a reticle and lens to a silicon wafer. Only a small area can be exposed

Figure 1.2: Current model stepper (Courtesy of [66]).

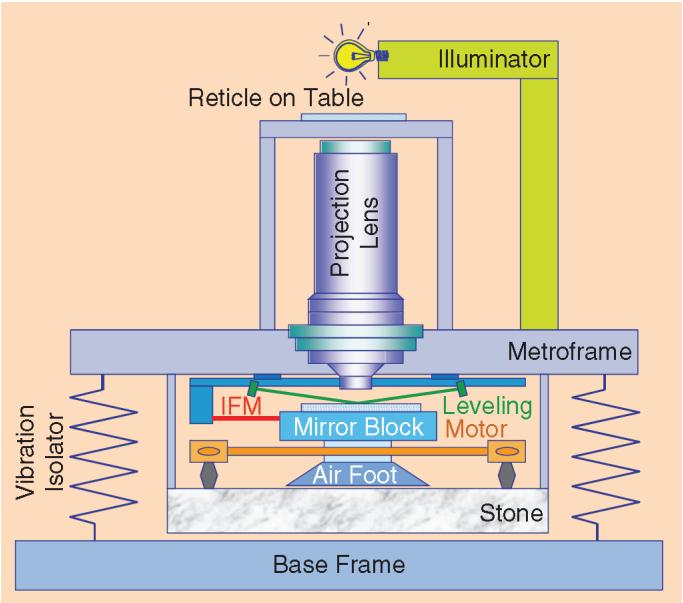

Figure 1.3: Stepper layout (Courtesy of [8]).

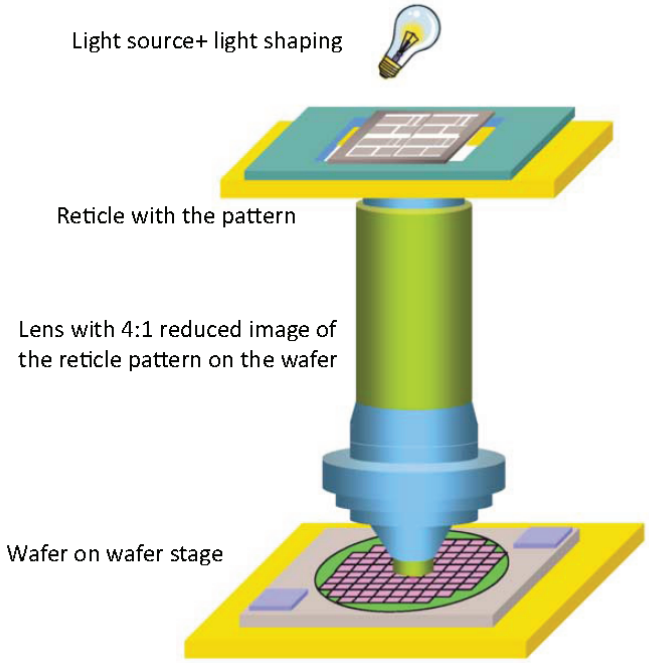

Figure 1.4: Schematic drawing of the main components of a wafer stepper (Courtesy of [58]).

in one exposure time. It means that the wafer has to be exposed by several steps while it must be positioned accurately between the different exposures by the wafer stage. This stepping motion has to be done extremely fast to save time and keep the productivity on an acceptable level.

1.2.2 Scanner

Instead of the step-and-expose principle described in the stepper, each exposure is created by scanning the wafer through the illuminated narrow slit in the step-and-scan method. Figure 1.5 shows the current model scanner produced by ASML and Figure 1.6 shows the scanner layout. Figure 1.7 shows the step-and-scan principle during exposing a whole wafer. Hence, a larger image can be created with the same projection lens by using the step-and-scan method. This lithographic scanner was brought to market around 1997 [7]. The major implications in the transition from stepper to scanner are described below.

Figure 1.5: Current model scanner (Courtesy of [67]).

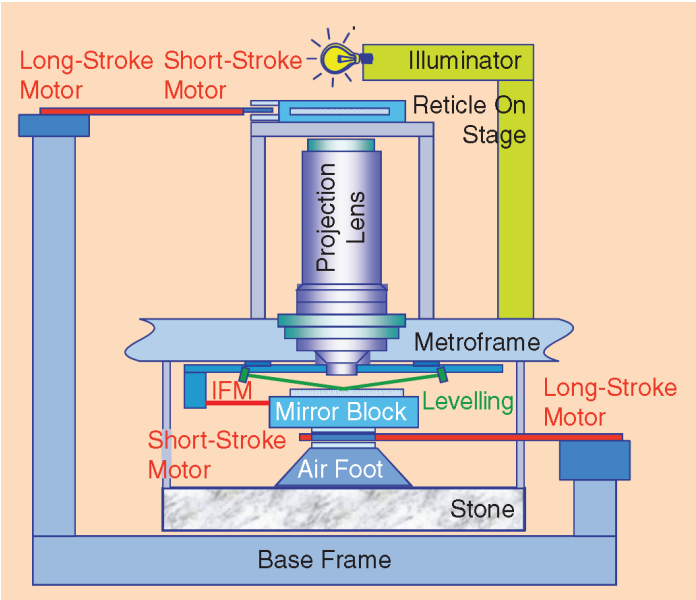

Figure 1.6: Scanner layout (Courtesy of [8]).

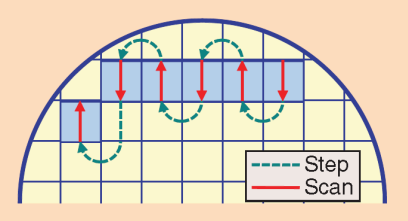

Figure 1.7: The step-and-scan principle in exposing a wafer (Courtesy of [8]).

Figure 1.8: Current model dual-stage scanner (Courtesy of [68]).

The main difference between the stepper and scanner is that the scanner in the presence of a reticle stage that can move the reticle in synchronization with the wafer. Small positioning errors with respect to the setpoint must be guaranteed during the constant-velocity scan, requiring changes in actuator concepts, guiding, and motion controller timing [8].

1.2.3 Dual-stage scanner

Around the year 2000, a wafer size change from a 200 mm to a 300 mm diameter is required by the semiconductor manufacturing industry to enable placement of more than twice the amount of chips on each wafer. Simultaneously, the chip

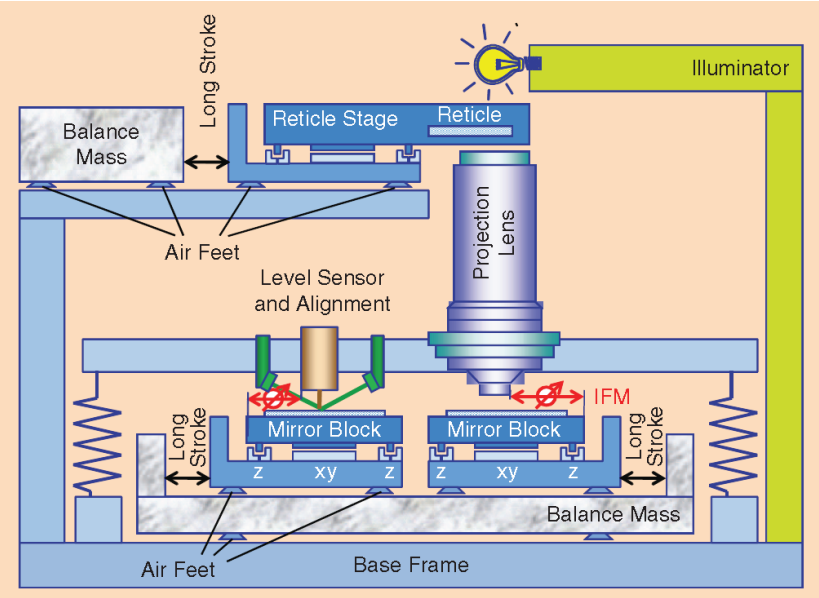

Figure 1.9: Dual-stage scanner layout (Courtesy of [8]).

design shrink continued, demanding higher positioning accuraciy for the stages. This change implies that the stages have to support larger 300 *mm* wafers, have to become faster to keep the productivity per hour, and have to become more accurate to enable smaller minimum feature sizes [8].

A solution was found by equipping the system with two wafer stages [68]. While the first stage exposes the wafer, the second stage unloads the previous wafer from the tool, loads a new wafer on the stage, aligns the horizontal placement of the wafer on the stage, and measures the wafer height map used to focus the wafer during exposure. When both stages are finished with their tasks, the stages are swapped and a new cycle begins [8]. The increased stage acceleration and speed further improves throughput.

ASMLs TWINSCAN NXE platform is the industrys first production platform for extreme ultraviolet lithography (EUVL). Figure 1.8 shows a commercially available lithographic tool, while Figure 1.9 shows a dynamic layout of a dual-stage scanner.

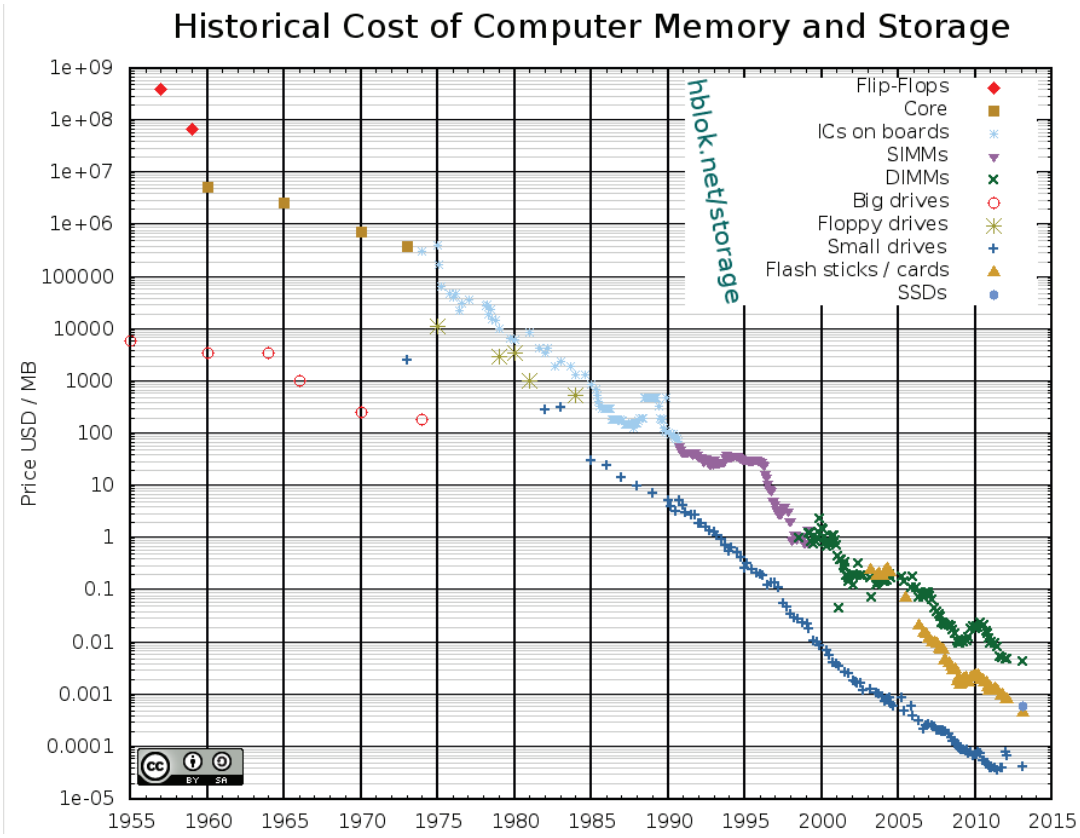

Figure 1.10: Historical cost of computer memory and storage (Courtesy of [52]).

1.3 Challenge to the next-generation fine stage actuator

As discuss above, these devices use an optical system to form an image of a pattern on a quartz plate, called the reticle placed on reticle stage, onto a photosensitive layer on a substrate, called the wafer placed on wafer stage. Because of exposure is done during quick synchronous scanning between reticle stage and wafer stage, both high acceleration and nanometer level precision is required. Usually, reticle and wafer stage use coarse and fine two layer structure [8] to achieve high acceleration and high precision. The coarse stage moves in long stroke with high acceleration to realize micrometer level positioning precision, and fine stage moves in short stroke to realize nanometer-level positioning precision. Therefore, the fine stage is playing the key role in lithography.

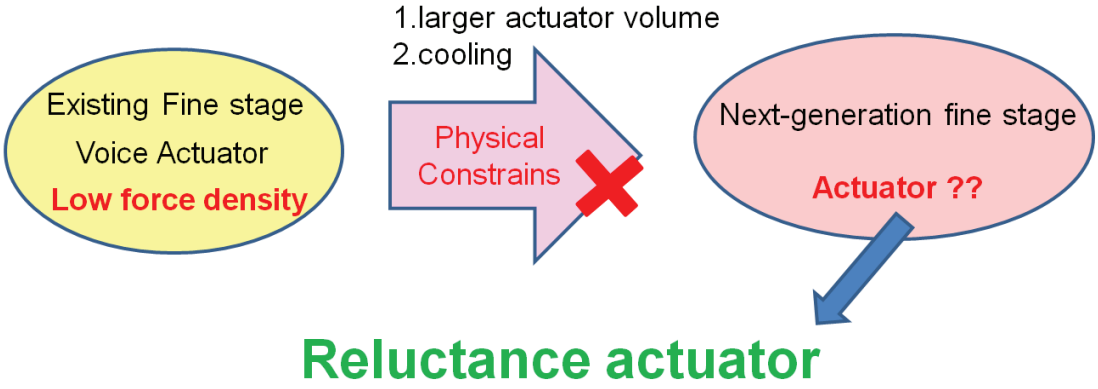

Figure 1.11: Voice actuator and reluctance actuator.

Moore's law, which states that every one and a half to two years the computing power per chip doubles, has held steady for four decades [56]. Figure 1.10 shows an example the historical cost of computer memory and storage [52] from 1955-2014, which amounts to a thousand-fold decrease in slightly over ten years. The more functionality packed into each IC, the smaller feature size required, which indicate the smallest component that can be manufactured in one IC. Today, the minimum feature size is about 15 nm [79], and it is foreseeable that it will be smaller in the future. And the chip manufacturers continually process a large number of wafer per hour to gain more profit. These requirements make the lithographic tools challenging from a position-control perspective with high speed, high acceleration and nano-positioning precision. The high speed and acceleration needed for wafer and reticle motion are in most cases provided by linear motors that exert reaction forces on the support structure.

In order to achieve the above requirements, the fine stage must have a light mass, and a high stiffness for high bandwidth control performance. Voice coil actuator is widely used as a driving actuator for fine stage due to the small size, low disturbance and high response frequency characteristic. But its drawback is the low efficiency and high power dissipation. With lithography emerging as the central technology for 15 nm nodes and beyond, the accuracy and throughput requirements demanded from next generation lithography is stringent, which means that higher acceleration and precision of fine stage are needed. If voice coil actuator is still used to achieve greater force, its size will become very large

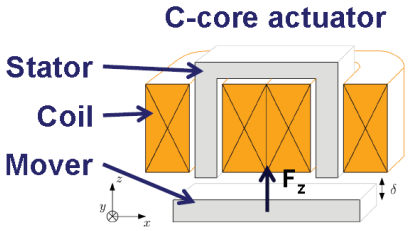

Figure 1.12: C-core reluctance actuator.

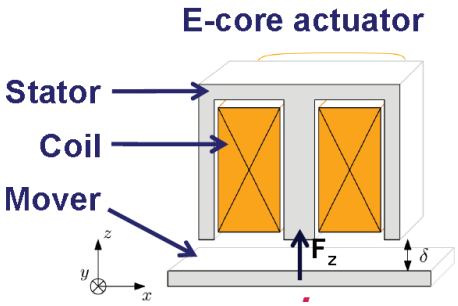

Figure 1.13: E-core reluctance actuator.

and the heat dissipation problem will be very difficult to solve [84]. Therefore, the voice coil actuator is no longer the best choice as the main driving actuator of fine stage. To break through this spiral, the reluctance actuator can provide a solution. Two reluctance actuators are considered in this thesis. One has a Cobalt-Iron C-core and 2 excitations coils as shown in figure 1.12. One has a Cobalt-Iron E-core and 3 excitations coils as shown in figure 1.13.

1.4 Reluctance linear actuator and hysteresis control

1.4.1 Reluctance linear actuator

The force density and accuracy must increase to improve the throughput and to obtain a precision in the nanometer range. The force density of the moving mass over a short-stroke (millimeter range), is increased by the use of reluctance actuators as shown in Figure 1.12, and 1.13 which are able to achieve a more than 10 times higher force density than frequently applied voice-coil actuators.

Since the variable reluctance force is proportional to the square of the excitation current, the reluctance actuator can produce greater force with a small volume and low current than the linear voice coil actuators. It brings about obvious advantages in the maximal obtainable force to current ratios. On the other hand, input to output non-linearity, the purely attractive nature of the reluctance force, parasitic magnetic effects like hysteresis [6] put limitations on the high-precision positioning applications. For the nonlinear current-force and position-force a nonlinear actuator model can be applied. However, magnetic hysteresis is nonlinear, rate-dependent and history dependent. So the hysteresis has to be studied to obtain a predictable force to meet required position accuracy in nano-positioning precision.

1.4.2 Hysteresis compensation control based on the inverse hysteresis model

Many systems can be modeled with a hysteresis element at the input. A feedforward compensator [32] constructs a hysteresis inverse which compensates the hysteresis together with the feedback control. The disturbance, which is caused by hysteresis, is reduced and better closed-loop performance can be achieved [11]. Compensation for hysteresis and boost performance of systems was applied with smart actuators successfully [53][88][33]. The adaptive control method was used to compensate the hysteresis in [18]. Although there exits many hysteresis compensation method, the compensation method for reluctance actuator with hysteresis is rare. In [54] a reluctance actuator was modeled and inverted using the classical Preisach model. This approach showed improved linearity, but was computationally complex and was tested only for periodic inputs. Paper [38] using the inverse hysteresis model to compensate the reluctance with hysteresis has provided a better performance. However, the above compensation method also need to have the hysteresis model.

1.5 Research objectives

1.5.1 The main features

In this thesis, the main objective is to study the hysteresis compensation method for the reluctance linear actuator with hysteresis. The main features of the proposed methods is that they do not need the hysteresis models.

1.5.2 The main contributions

The main contributions of this thesis are as follows:

1. The models without hysteresis for C-core and E-core reluctance linear actuator are reviewed and then the reluctance linear actuator models with hysteresis are proposed.

2. A hysteresis current compensation configuration [48] for the reluctance linear actuator with hysteresis is proposed based on the adaptive multi-layer neural network, which is used as a learning machine of hysteresis.

3. A new nonlinear control method [47] is proposed for the stage having paired reluctance linear actuator with hysteresis using the direct adaptive neural network, which is used as a learning machine of nonlinearity. The feature of this method lies in that the nonlinear compensator in conventional methods, which computed the current reference from that of the input and output force, is not used. This naturally overcomes the robustness issue with respect to parameter uncertainty.

4. Acceleration feedback is designed for the fine stage having paired reluctance linear actuator with hysteresis. The feature of this method lies in that by considering the hysteresis force as a disturbance force, we can design an acceleration feedback loop to reduce the influence of the hysteresis force. The proposed method can improve the process sensitivity for low frequencies and remove the high-bandwidth requirement. Acceleration feedback implementation in digital controller and control for a fine stage connected to a coarse stage are discussed.

Then we carry out the simulations to test the proposed compensation methods. The simulation results show that the proposed methods are effective in overcoming the hysteresis and promising in high-precision and high acceleration control applications.

1.6 Thesis layout

The thesis is organized as follows:

- **Chapter** 2 reviews the models without hysteresis for the C-core and E-Core reluctance linear actuators and proposes the models with hysteresis for the C-core and E-core reluctance linear actuators.
- **Chapter** 3 reviews the control method for the reluctance linear actuator.
- **Chapter** 4 proposes a hysteresis current compensation configuration for the reluctance linear actuator with hysteresis based on the adaptive multi-layer neural network.
- **Chapter** 5 proposes a new nonlinear control method for the stage having paired reluctance linear actuator with hysteresis using the direct adaptive neural network, which is used as a learning machine of nonlinearity.
- **Chapter** 6 designs the acceleration feedback for the fine stage having paired reluctance linear actuator with hysteresis. The feature of this method lies in that by considering the hysteresis force as a disturbance force to design the acceleration feedback loop, we can reduce the influence of the hysteresis force.

2

Reluctance Linear Actuator Models with Hysteresis

2.1 Introduction

In this chapter, the reluctance linear actuator models are discussed. The parametric hysteresis operator is reviewed in section 2.2; in section 2.3, models without hysteresis for reluctance linear actuator with C-core is reviewed and Models with hysteresis is proposed; in section 2.4, models without hysteresis for reluctance linear actuator with E-core is reviewed and the details of the derivation process are proposed.

2.2 Hysteresis model

2.2.1 Review of the hysteresis model

Hysteresis is a nonlinear effect that arises in diverse disciplines ranging from physics to biology, from material science to mechanics, and from electronics to economics. The study of hysteresis has a long history [83]. The word hysteresis was coined during the study of ferromagnetism in [19]; The rules for scalar hysteresis was discovered in [50]; Preisach model for scalar hysteresis was introduced in [65]; a hysteretic relationship between moisture content in the soil and capillary pressure is discovered in [30]. A fundamental economic phenomenon

with hysteresis was studied in [17] based on sunk-costs . Starting in 1970, the rate-independent hysteresis operators are studied in [63]. An understanding of general scalar hysteresis operators was proposed in [51][75] [40]. The need for better control motivates the need for identification and control methods for systems described by hysteresis operators [78] [23] [34] [77] [41] [44] [73][74]. In 2009, a special issue for modeling and control of hysteresis was published [45][37][4]. In this thesis, the hysteresis operator [39] will be used to model the reluctance actuator with hysteresis.

2.2.2 Parametric hysteresis operator

Hysteresis is encountered over a wide range of applications that usually involve magnetic, ferroelectric, mechanical, or optical systems. It is a complex nonlinearity that displays the properties of bifurcation and nonlocal memory. The hysteresis can be defined as a loop in the input−output map. In this paper, the parametric hysteresis operators [39] are reviewed, which is defined in the discrete time domain, so the implementation is more straightforward.

Definition 2.1. Let the indicator $\chi : \mathbb{R}^n, \mathbb{Z}^+ \to \mathbb{Z}^+$ be defined as:

$\chi(u,k) \equiv \chi_{u,k} = \sup\ K^*,$
$K^* = \{1 \cup k^* \mid [u(k^*) - u(k^* - 1)][u(k^* + 1) - u(k^*)] < 0\},$

where $k, k^* \in \mathbb{Z}^+, k^* < k$ and $u : \mathbb{Z}^+ \to \mathbb{R}^n$ is a discrete-time signal, $\mathbb{Z}^+$ denotes the set of positive integers, and n can be any integer larger than equal to k.

The indicator $\chi(u,k)$ outputs the last time instant before k when the discrete derivative of u changed sign, i.e. an extremum occurred. It only has to receive elements of the signal u up to the moment k, i.e. $u(1,...,k)$, since future values are not used.

Definition 2.2. Let $s : \mathbb{R}^n, \mathbb{Z}^+ \to \{-1, +1\}$ be an indicator defined as:
$s(u,k) \equiv s = \mathrm{sgn}^+[u(k) - u(\chi(u,k))]$
where sgn^+ is the right-continuous sign function. The indicator S determines whether the signal $u(k)$ is monotonically increasing or decreasing since the last extremum indicated by $\chi(u,k)$.

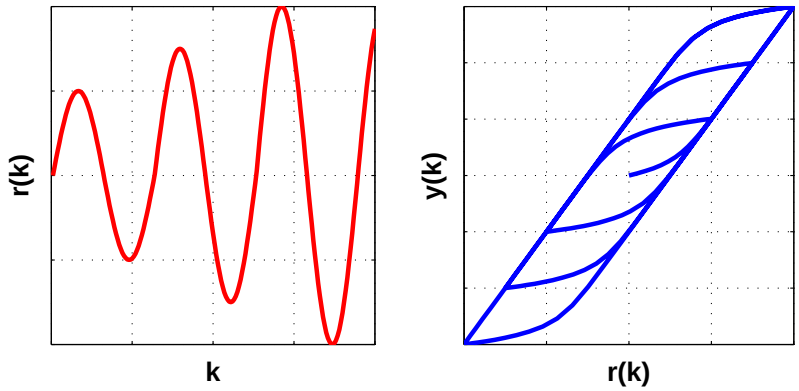

Figure 2.1: Input $r(k)$(left) and the corresponding output $y(k)$ map (right) trajectories of the parametric hysteresis operator.

Definition 2.3. Let $r(t), y(t) \in C^{\infty}$, $\lambda_1, \lambda_2 \in \mathbb{R}^+$. Then the *parametric hysteresis operator*:

$$y(k) = H_{hys}[r(k), \lambda_1, \lambda_2] \tag{2.1}$$

is defined via

$$y(k) = r(k) - r_0 + v_0 + s[\frac{1}{\lambda_2} W(\lambda_2 q \cdot e^{\lambda_2(q-|r(k)-r_0|)}) - q], \tag{2.2}$$

where $q = \lambda_1 + s(y_0 - r_0), r_0 = r(\chi(r,k))$ and $y_0 = y(\chi(r,k))$. W is the principal branch of the Lambert W function [14].

An input $r(k)$ and output $y(k)$ map of the parametric hysteresis operator are shown in Figure 2.1. The parameter λ_1 represents the amount of hysteresis around the straight line $r(k) = y(k)$ and defines the asymptotes, while the parameter λ_2 defines the smoothness of the hysteresis loops, i.e. the rate of convergence towards the left or right asymptote. The parametric hysteresis operator operates in two modes whose representations are shown in Figure 2.2.

Definition 2.4. Let $r(t), y(t) \in C^{\infty}$, $\lambda_1, \lambda_2, \in \mathbb{R}^+$. Then the *inverse hysteresis operator*:

$$y(k) = H^{-1}_{hys}[r(k), \lambda_1, \lambda_2] \tag{2.3}$$

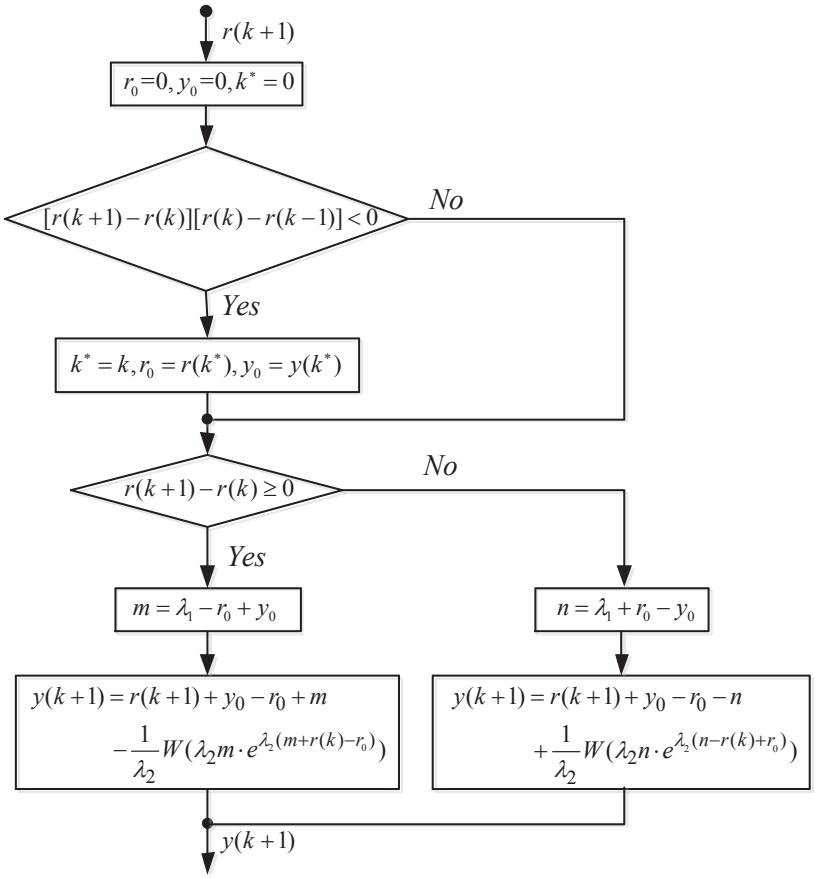

Figure 2.2: Automata representation of the hysteresis operator.

is defined via

$$y(k) = r(k) - r_0 + v_0 + sq(1 - e^{-\lambda_2|r(k)-r_0|}) \tag{2.4}$$

where $q = \lambda_1 + s(r_0 - y_0), r_0 = r(\chi(r,k))$ and $y_0 = y(\chi(r,k))$.

Remark 2.5. The inverse parametric hysteresis operator (2.4) can be split into a linear part and a hysteretic part as follows:

$$H_{hys}^{-1}[r(k), \lambda_1, \lambda_2] = r(k) + \varphi[r(k), \lambda_1, \lambda_2], \tag{2.5}$$

where the hysteretic part $\varphi(r(k), \lambda_1, \lambda_2)$ is:

$$y^*(k) = y_0^* + sq(1 - e^{-\lambda_2|r(k)-r_0|}) \tag{2.6}$$

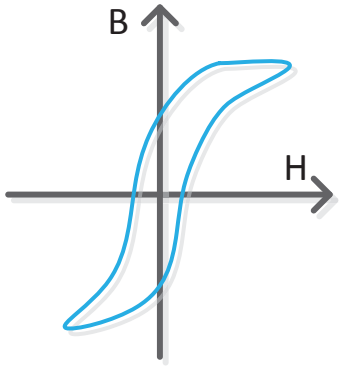

Figure 2.3: H and B curve.

with $q = \lambda_1 - sv_0^*, r_0 = r(\chi(r,k))$ and $v_0^* = v^*(\chi(r,k))$.

Propostion 2.6. For the hysteretic part φ of the inverse parametric hysteresis operator defined in (2.6), $\forall a, b > 0$ the following holds:

$$\lim_{r\to\infty}\{a\cdot\varphi[b\cdot r(k),\lambda_1,\lambda_2]-\varphi[r(k),a\cdot\lambda_1,b\cdot\lambda_2]\}\to 0 \tag{2.7}$$

under the persistent excitation criterion that $r(k) - r(k-1)$, only at a finite number of time instants k, i.e. the input $u(k)$ is non-constant.

2.2.3 H and B model using hysteresis operator

However, the E-core coil uses the soft magnetic material, which has magnetic hysteresis [6] between the magnetic field H_{fe} and the bulk magnetic flux density B_{fe}. The typical B_{fe}–H_{fe} curve is illustrated in Figure 2.3. It is assumed that the hysteretic B_{fe}–H_{fe} curve and the H_{fe}–B_{fe} curve of the core material can be modeled [39] by the parametric hysteresis operator Equation (2.1) and the inverse hysteresis operator Equation (2.3). Furthermore, since the input and output of the hysteresis operators have to be in the same physical units, B_{fe} will be scaled with $\frac{1}{\mu_0\mu_r}$. Then, we get the B_{fe}–H_{fe} curve model:

$$B_{fe} = H_{hys}(\mu_0\mu_r H_{fe},\lambda_1,\lambda_2) \tag{2.8}$$

and H_{fe}–B_{fe} curve model:

$$H_{fe} = H_{hys}^{-1}(\frac{B_{fe}}{\mu_0\mu_r},\lambda_1,\lambda_2). \tag{2.9}$$

2.3 Models for reluctance linear actuator with C-core

2.3.1 Magnetism principle

A brief introduction or review of magnetism will establish the basic ideas and nomenclature exploited in the remainder of this discussion of electromagnets.

The total magnetic flux Φ passing through a surface A is the integral of flux density B over the surface:

$$\Phi = \iint_A B \cdot dA. \tag{2.10}$$

The magnetic field H and the magnetic induction (flux density) B are linked by the *constitutive law*:

$$B = \mu_0 \mu_r H. \tag{2.11}$$

Here, $\mu_0 = 4\pi \times 10^{-7} Vs/Am$ stands for the *magnetic permeability* of a vacuum. The *relative permeability* μ_r depends on the medium upon which the magnetic field acts. For a vacuum, μ_r equals 1 and is also approximately unity in the air. The SI unit of the magnetic field H is A/m.

2.3.2 Magnetic circuit

In the magnetic bearing technology, electromagnets or permanent magnets cause the flux to circulate in a magnetic loop. When analyzing such magnetic loops, an exact theoretical computation of the field is rarely possible and seldom required. One usually works with analytic methods of approximation, based on the simplifying assumption that the flux, except for in the air gap, runs entirely through the iron (no leakage flux).

The field within the magnetic loop is assumed to be homogeneous both in the iron and in the air gap. Therefore, we base our calculation on a mean length l_{fe} of the magnetic path and an air gap length of $2x_g$.

For the magnetic circuit in Figure 2.4

$$\oint H \cdot dl = l_{fe} H_{fe} + 2x_g H_a = Ni \tag{2.12}$$

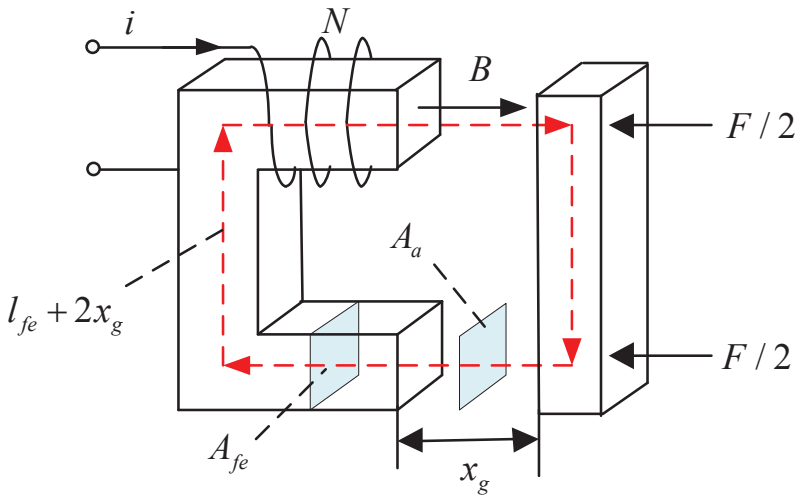

Figure 2.4: C-core I Magnetic circuit.

Follows from *Amperes circuital law*. From the flux density B_{fe} in the iron and B_a in the air gap, field intensities H_{fe} and H_a from Equation (2.12) can be replaced by Equation (2.11):

$$\frac{l_{fe}}{\mu_0 \mu_r} \cdot B_{fe} + \frac{2x_g}{\mu_0} \cdot B_a = Ni. \tag{2.13}$$

2.3.3 Flux density without hysteresis

Since the permeability $\mu = \mu_0 \mu_r$ of iron is considerably larger than that of air, the magnetic field lines leave the iron almost perpendicularly to its surface. Both for constant and alternating fields the computational methods used for static fields are applied, which is admissible as long as the alternating fields have a very large wavelength, compared with the geometry of the field.

For the computation of flux density B, the following simplifying assumptions are made: Flux Φ runs entirely within the magnetic loop with iron cross section A_{fe} which is assumed to be constant along the entire loop and equal to cross-

section A_a in the air gap. From

$$\Phi = B_{fe}A_{fe} = B_aA_a \tag{2.14}$$

and

$$A_{fe} = A_a, \tag{2.15}$$

it follows that

$$B_{fe} = B_a. \tag{2.16}$$

Solving Equation (2.13) for B_a yields

$$B_a = \mu_0 \frac{Ni}{(\frac{l_{fe}}{\mu_r} + 2x_g)}. \tag{2.17}$$

In the iron, $\mu_r \gg 1$, so the magnetization of the iron is often neglected. In this case, Equation (2.17) may be simplified to:

$$B_a = \mu_0 \frac{Ni}{2x_g}. \tag{2.18}$$

2.3.4 Energy in the air gaps

In this section, the simple reluctance actuator with a C-Core, as shown in Figure 2.4 is discussed.

The attraction force of magnets is generated at the boundaries between differing permeability μ. The calculation of these forces is based on the field energy. We consider the energy W_a stored in the volume of the air gap, $V_a = 2x_gA_a$. In the case of the homogeneous field in the air gap of the magnetic loop, as represented in Figure 2.4, the stored energy W_a obeys

$$W_a = \frac{1}{2}B_aH_aV_a \tag{2.19}$$

$$= \frac{1}{2}B_aH_aA_a(2x_g). \tag{2.20}$$

In the following, we will discuss how to get the $B_a(i, x_g)$.

2.3.5 Magnetic force without hysteresis

The force acting on the ferromagnetic body ($\mu_r \gg 1$) is generated by a change of the field energy in the air gap, as a function of the body displacement. For small displacements d_s the magnetic flux $B_a A_a$ remains constant.

When the air gap s increases by dx_g, the volume increases by $dV_a = 2dx_g A_a$, and the energy W_a in the field increases by dW_a. This energy has to be provided mechanically, i.e. an attractive force has to be overcome. Thus, the force F equals the partial derivative of the field energy W_a with respect to the air gap x_g (principle of virtual displacement):

$$F = -\frac{\partial W_a}{\partial x_g} \tag{2.21}$$

$$= B_a H_a A_a = \frac{B_a^2 A_a}{\mu_0}. \tag{2.22}$$

In the case of a closed system, the force F can be derived from the principle of virtual displacement. For electromagnets (Figure 2.4), electric energy is introduced into the system through the coil terminals to set up the magnetic field. In order for Equation (2.22) to remain valid, the differentiation has to be carried out as if there is no electric energy exchange between the coil and its power supply, i.e. when the flux density B remains constant. To derive force F as a function of coil current and the air gap, $B_a(i, x_g)$ is inserted into Equation (2.22) after differentiating.

To include the effect of iron with a constant, finite permeability μ_r, Equation (2.18) will replace B_a in Equation (2.22). The force F resulting in this case, is

$$F = \mu_0 \Big(\frac{Ni}{l_{fe}/\mu_r + 2x_g} \Big)^2 A_a. \tag{2.23}$$

Neglecting the Iron

In the simplest case where the iron is neglected, B_a is replaced by Equation (2.17). From Equation (2.22), the resulting force F is

$$F = \mu_0 A_a (\frac{Ni}{2x_g})^2 = \frac{1}{4}\mu_0 N^2 A_a \frac{i^2}{x_g^2} = \eta \frac{i^2}{x_g^2} \tag{2.24}$$

in which $\eta = \frac{1}{4}\mu_0 N^2 A_a$, and the area A_a is assumed to be the projected area of the pole face, rather than the curved surface area.

2.3.6 Flux density with hysteresis

From $H_a = \frac{B_a}{\mu_0}$ and by substituting Equation (2.9), Equation (2.13) is rewritten as:

$$i = \frac{2x_g}{\mu_0 N} \cdot B_a + \frac{l_{fe}}{N} \cdot H_{hys}^{-1}(\frac{B_{fe}}{\mu_0 \mu_r}, \lambda_1, \lambda_2). \tag{2.25}$$

From Equation (2.16), Equation (2.25) can be rewritten as:

$$i = \frac{2x_g}{\mu_0 N} \cdot B_a + \frac{l_{fe}}{N} \cdot H_{hys}^{-1}(\frac{B_a}{\mu_0 \mu_r}, \lambda_1, \lambda_2). \tag{2.26}$$

Splitting the hysteresis operator in Equation (2.26) as in Equation (2.5) yields:

$$i = \frac{B_a}{\mu_0 N}(2x_g + \frac{l_{fe}}{\mu_r}) + \frac{l_{fe}}{N} \cdot \varphi(\frac{B_a}{\mu_0 \mu_r}, \lambda_1, \lambda_2). \tag{2.27}$$

After appling Proposition 2.6, Equation (2.27) becomes:

$$\begin{aligned} i &= \frac{B_a}{\mu_0 N}(2x_g + \frac{l_{fe}}{\mu_r}) + \varphi\Big(\frac{B_a}{\mu_0 N}(2x_g + \frac{l_{fe}}{\mu_r}), \lambda_1^*, \lambda_2^*\Big) \\ &= H_{hys}^{-1}\Big(\frac{B_a}{\mu_0 N}(2x_g + \frac{l_{fe}}{\mu_r}), \lambda_1^*, \lambda_2^*\Big). \end{aligned} \tag{2.28}$$

where $\lambda_1^* = \frac{l_{fe}}{N}\lambda_1$ and $\lambda_2^* = \frac{1}{(\frac{2x_g \mu_r A_{fe}}{A_a} + l_{fe})}\lambda_2$. Then from Equation (2.28), we get:

$$B_a = \frac{\mu_0 N}{2x_g + \frac{l_{fe}}{\mu_r}} \cdot H_{hys}(i, \lambda_1^*, \lambda_2^*). \tag{2.29}$$

In the iron, $\mu_r \gg 1$, so the magnetization of the iron is often neglected, then Equation (2.29) may be simplified as:

$$B_a = \frac{\mu_0 N}{2x_g} \cdot H_{hys}(i, \lambda_1^*, \lambda_2^*). \tag{2.30}$$

2.3.7 Magnetic force with hysteresis

Then by substituting Equation (2.30) into Equation (2.22), a new reluctance actuator model with hysteresis is obtained as:

$$F = \frac{\mu_0 A_a N^2}{4} \cdot \frac{(H_{hys}(i, \lambda_1^*, \lambda_2^*))^2}{x_g^2}. \tag{2.31}$$

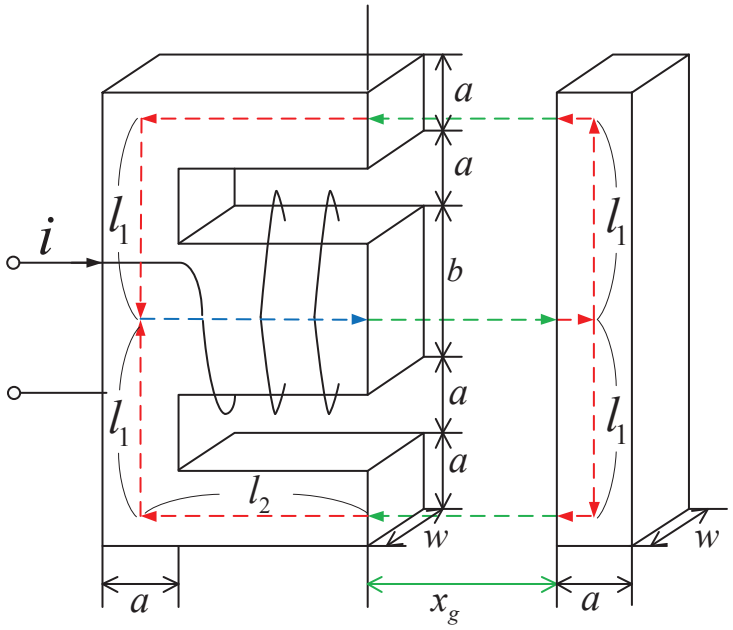

Figure 2.5: E-core structure.

Neglecting the Iron

By substituting Equation (2.29) into Equation (2.22), a new reluctance actuator model with hysteresis is obtained as:

$$F = \mu_0 A_a N^2 \cdot \frac{(H_{hys}(i, \lambda_1^*, \lambda_2^*))^2}{(2x_g + \frac{l_{fe} A_a}{\mu_r A_{fe}})^2}. \tag{2.32}$$

2.4 Models for reluctance linear actuator with E-core

In this section, the models for reluctance linear actuator with E-core as shown in figure 2.5 is discussed.

2.4.1 Magnetic circuit

For the magnetic circuit in Figure 2.5, it follows from *Amperes circuital law* that

$$Ni = H_{fe1} \cdot l_2 + H_{fe5} \cdot l_1 + H_{fe7} \cdot l_1 + H_{a1} \cdot x_g$$

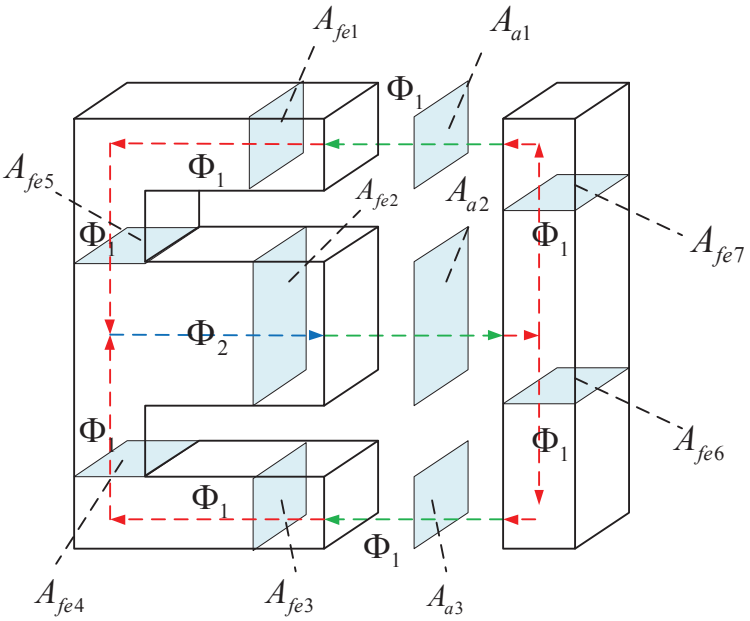

Figure 2.6: E-core flux circuit

$$
\begin{aligned}
&+ \quad H_{fe2} \cdot l_2 + H_{a2} \cdot x_g \\
&+ \quad H_{fe4} \cdot l_1 + H_{fe3} \cdot l_2 + H_{fe6} \cdot l_1 + H_{a3} \cdot x_g \\
&+ \quad H_{fe2} \cdot l_2 + H_{a2} \cdot x_g
\end{aligned} \tag{2.33}
$$

From the flux density B_{fe} in the iron and B_a in the air gap, field intensities H_{fe} and H_a from Equation (2.33) can be replaced by Equation (2.11):

$$
\begin{aligned}
Ni \quad = \quad & \frac{B_{fe1}}{\mu_0\mu_r} \cdot l_2 + \frac{B_{fe5}}{\mu_0\mu_r} \cdot l_1 + \frac{B_{fe7}}{\mu_0\mu_r} \cdot l_1 + \frac{B_{a1}}{\mu_0} \cdot x_g \\
+ \quad & \frac{B_{fe2}}{\mu_0\mu_r} \cdot l_2 + \frac{B_{a2}}{\mu_0} \cdot x_g \\
+ \quad & \frac{B_{fe4}}{\mu_0\mu_r} \cdot l_1 + \frac{B_{fe3}}{\mu_0\mu_r} \cdot l_2 + \frac{B_{fe6}}{\mu_0\mu_r} \cdot l_1 + \frac{B_{a3}}{\mu_0} \cdot x_g \\
+ \quad & \frac{B_{fe2}}{\mu_0\mu_r} \cdot l_2 + \frac{B_{a2}}{\mu_0} \cdot x_g.
\end{aligned} \tag{2.34}
$$

2.4.2 Flux density without hysteresis

For the computation of flux density B, from Figure 2.5, a flux circuit as shown in Figure 2.6, the following simplifying assumptions are made: Flux Φ runs entirely within the magnetic loop with iron cross section A_{fe1}, A_{fe3}, A_{fe4}, A_{fe5},A_{fe6}, A_{fe7}, which are assumed to be constant along the entire loop and equal to cross-section A_{a1} and A_{a3} in the air gap, we get:

$$\begin{aligned} \Phi_1 &= B_{fe1}A_{fe1} \\ &= B_{fe3}A_{fe3} \\ &= B_{fe4}A_{fe4} \\ &= B_{fe5}A_{fe5} \\ &= B_{fe6}A_{fe6} \\ &= B_{fe7}A_{fe7} \\ &= B_{a1}A_{a1} \\ &= B_{a3}A_{a3} \end{aligned} \tag{2.35}$$

$$\begin{aligned} A_a &= A_{fe1} \\ &= A_{fe3} \\ &= A_{fe4} \\ &= A_{fe5} \\ &= A_{fe6} \\ &= A_{fe7} \\ &= A_{a1} \\ &= A_{a3}, \end{aligned} \tag{2.36}$$

Let B_{fe} be the flux density in the iron, then

$$\begin{aligned} B_fe &= B_{fe1} \\ &= B_{fe3} \\ &= B_{fe4} \\ &= B_{fe5} \end{aligned}$$

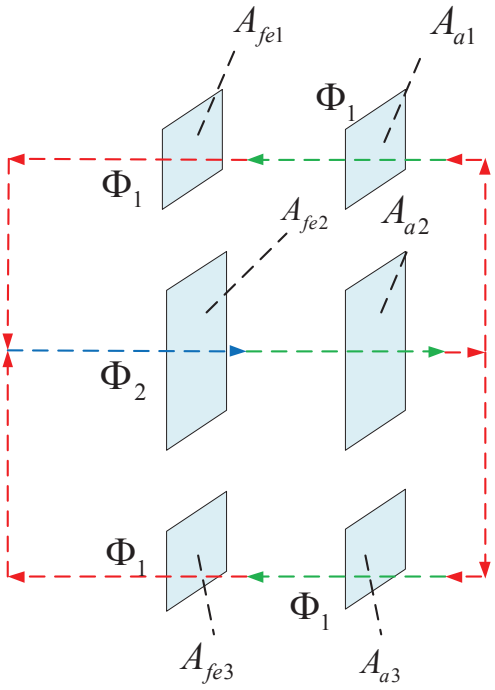

Figure 2.7: Simplified flux circuit

$$\begin{aligned} &= B_{fe6} \\ &= B_{fe7}. \end{aligned} \tag{2.37}$$

Further, B_a be the flux density in the air gap and

$$\begin{aligned} B_a &= B_{a1} \\ &= B_{a3}. \end{aligned} \tag{2.38}$$

Then from Equations (2.35), (2.36), (2.37) and (2.38), we get

$$B_{fe} = B_a. \tag{2.39}$$

From Equations (2.35), (2.36), (2.37), (2.38) and (2.39) and Figure 2.6, a simplified flux circuit is shown in Figure 2.7, in which

$$\begin{aligned} \Phi_1 &= B_{fe} A_a \\ &= B_a A_a. \end{aligned} \tag{2.40}$$

Then from Figure 2.6, we get:

$$\begin{aligned} \Phi_2 &= 2\Phi_1 \\ &= 2B_{fe}A_a \\ &= 2B_aA_a. \end{aligned} \tag{2.41}$$

When $b = a$ as shown in Figure 2.5:

$$A_{fe2} = A_{a2} = A_a \tag{2.42}$$

Then from Equation (2.41) and (2.42), we get:

$$B_{fe2} = B_{a2} \tag{2.43}$$

$$B_{fe2} = 2B_{fe} \tag{2.44}$$

$$B_{a2} = 2B_a \tag{2.45}$$

From Equations (2.37), (2.38), (2.44) and(2.45), Equation (2.34) can be rewritten as:

$$\begin{aligned} Ni &= \frac{B_{fe}}{\mu_0\mu_r}\cdot l_2 + \frac{B_{fe}}{\mu_0\mu_r}\cdot l_1 + \frac{B_{fe}}{\mu_0\mu_r}\cdot l_1 + \frac{B_a}{\mu_0}\cdot x_g \\ &+ \frac{2B_{fe}}{\mu_0\mu_r}\cdot l_2 + \frac{2B_a}{\mu_0}\cdot x_g \\ &+ \frac{B_{fe}}{\mu_0\mu_r}\cdot l_1 + \frac{B_{fe}}{\mu_0\mu_r}\cdot l_2 + \frac{B_{fe}}{\mu_0\mu_r}\cdot l_1 + \frac{B_a}{\mu_0}\cdot x_g \\ &+ \frac{2B_{fe}}{\mu_0\mu_r}\cdot l_2 + \frac{2B_a}{\mu_0}\cdot x_g. \end{aligned} \tag{2.46}$$

Define $l_{m1} = 4l_1 + 6l_2$. Equation (2.46) can be rewritten as:

$$Ni = \frac{B_{fe}}{\mu_0\mu_r}\cdot l_{m1} + \frac{B_a}{\mu_0}\cdot 6x_g. \tag{2.47}$$

Then, from Equation (2.47) and (2.39), B_a becomes:

$$B_a = \frac{Ni\mu_0}{\frac{l_{m1}}{\mu_r} + 6x_g}. \tag{2.48}$$

In the iron, $\mu_r \gg 1$, so the magnetization of the iron is often neglected. In this case, Equation (2.48) may be simplified:

$$B_a = \frac{Ni\mu_0}{6x_g} \tag{2.49}$$

When $b = 2a$ as shown in Figure 2.5:

$$A_{fe2} = A_{a2} = 2A_a \tag{2.50}$$

Then from Equation (2.41) and (2.50), we get:

$$B_{fe2} = B_{a2} \tag{2.51}$$

$$B_{fe2} = B_{fe} \tag{2.52}$$

$$B_{a2} = B_a. \tag{2.53}$$

From Equations (2.37), (2.38), (2.52) and(2.53), Equation (2.34) can be rewritten as:

$$\begin{aligned} Ni &= \frac{B_{fe}}{\mu_0\mu_r}\cdot l_2 + \frac{B_{fe}}{\mu_0\mu_r}\cdot l_1 + \frac{B_{fe}}{\mu_0\mu_r}\cdot l_1 + \frac{B_a}{\mu_0}\cdot x_g \\ &+ \frac{B_{fe}}{\mu_0\mu_r}\cdot l_2 + \frac{B_a}{\mu_0}\cdot x_g \\ &+ \frac{B_{fe}}{\mu_0\mu_r}\cdot l_1 + \frac{B_{fe}}{\mu_0\mu_r}\cdot l_2 + \frac{B_{fe}}{\mu_0\mu_r}\cdot l_1 + \frac{B_a}{\mu_0}\cdot x_g \\ &+ \frac{B_{fe}}{\mu_0\mu_r}\cdot l_2 + \frac{B_a}{\mu_0}\cdot x_g. \end{aligned} \tag{2.54}$$

Define $l_{m2} = 4l_1 + 4l_2$. Equation (2.54) can be rewritten as:

$$Ni = \frac{B_{fe}}{\mu_0\mu_r}\cdot l_{m2} + \frac{B_a}{\mu_0}\cdot 4x_g, \tag{2.55}$$

From Equation (2.55) and (2.39), B_a turns to:

$$B_a = \frac{Ni\mu_0}{\frac{l_{m2}}{\mu_r} + 4x_g}. \tag{2.56}$$

In the iron, $\mu_r \gg 1$, so the magnetization of the iron is often neglected. In this case, Equation 2.56 may be simplified as:

$$B_a = \frac{Ni\mu_0}{4x_g}. \tag{2.57}$$

2.4.3 Energy in the air gaps

In the case of homogeneous field in the air gap of the magnetic loop, as represented in Figure 2.5, the stored energy W_a obeys:

$$\begin{aligned} W_a &= \frac{1}{2}B_{a1}H_{a1}V_{a1} + \frac{1}{2}B_{a2}H_{a2}V_{a2} + \frac{1}{2}B_{a3}H_{a3}V_{a3} \\ &= \frac{1}{2}\Big(B_{a1}H_{a1}A_{a1} + \frac{1}{2}B_{a2}H_{a2}A_{a2} + \frac{1}{2}B_{a3}H_{a3}A_{a3}\Big)x_g \\ &= \frac{1}{2}\Big(\frac{B_{a1}^2}{\mu_0}A_{a1} + \frac{B_{a2}^2}{\mu_0}A_{a2} + \frac{B_{a3}^2}{\mu_0}A_{a3}\Big)x_g \end{aligned} \tag{2.58}$$

When $b = a$ as shown in Figure 2.5:
From (2.36), (2.38), (2.42), (2.45), Equation (2.58) can be rewritten as

$$\begin{aligned} W_a &= \frac{1}{2}\Big[\frac{B_a^2}{\mu_0}A_a + \frac{(2B_a)^2}{\mu_0}A_a + \frac{B_a^2}{\mu_0}A_a\Big]x_g \\ &= \frac{3B_a^2A_ax_g}{\mu_0}. \end{aligned} \tag{2.59}$$

When $b = 2a$ as shown in Figure 2.5:
From (2.36), (2.38), (2.50), (2.53), Equation (2.58) can be rewritten as

$$\begin{aligned} W_a &= \frac{1}{2}\Big[\frac{B_a^2}{\mu_0}A_a + \frac{B_a^2}{\mu_0}2A_a + \frac{B_a^2}{\mu_0}A_a\Big]x_g \\ &= \frac{2B_a^2A_ax_g}{\mu_0}. \end{aligned} \tag{2.60}$$

2.4.4 Magnetic force without hysteresis

When $b = a$ as shown in Figure 2.5:
From Equation (2.59), force F equals the partial derivative of the field energy W_a with respect to the air gap x_g (principle of virtual displacement):

$$F = -\frac{\partial W_a}{\partial x_g} = \frac{3B_a^2A_a}{\mu_0}. \tag{2.61}$$

From Equation (2.48) and (2.61), we get:

$$F = 3N^2\mu_0A_a\frac{i^2}{(\frac{l_{m1}}{\mu_r} + 6x_g)^2}. \tag{2.62}$$

Neglecting the Iron

From Equation (2.49) and (2.61), we get:

$$F = \frac{1}{12} N^2 \mu_0 A_a \frac{i^2}{x_g^2}. \tag{2.63}$$

When $b = 2a$ as shown in Figure 2.5:

From Equation (2.60), force F equals the partial derivative of the field energy W_a with respect to the air gap x_g (principle of virtual displacement):

$$F = -\frac{\partial W_a}{\partial x_g} = \frac{2B_a^2 A_a}{\mu_0} \tag{2.64}$$

From Equation (2.56) and (2.64), we get:

$$F = 2N^2 \mu_0 A_a \frac{i^2}{(\frac{l_{m2}}{\mu_r} + 4x_g)^2}. \tag{2.65}$$

Neglecting the Iron

From Equation (2.57) and (2.64), we get:

$$F = \frac{1}{8} N^2 \mu_0 A_a \frac{i^2}{x_g^2}. \tag{2.66}$$

2.4.5 Flux density with hysteresis

When $b = a$ as shown in Figure 2.5:

By substituting Equation (2.9), Equation (2.47) becomes:

$$i = \frac{B_a}{\mu_0 N} \cdot 6x_g + \frac{l_{m1}}{N} \cdot H_{hys}^{-1}\Big(\frac{B_{fe}}{\mu_0 \mu_r}, \lambda_1, \lambda_2\Big). \tag{2.67}$$

Splitting the hysteresis operator in Equation (2.67) as in Equation (2.5) yields

$$i = \frac{B_a}{\mu_0 N}(6x_g + \frac{l_{m1}}{\mu_r}) + \frac{l_{m1}}{N} \cdot \varphi(\frac{B_a}{\mu_0 \mu_r}, \lambda_1, \lambda_2). \tag{2.68}$$

After applying Proposition 1.6, Equation (2.68) becomes

$$\begin{aligned} i &= \frac{B_a}{\mu_0 N}(6x_g + \frac{l_{m1}}{\mu_r}) + \varphi(\frac{B_a}{\mu_0 N}(4x_g + \frac{l_{m1}}{\mu_r}), \lambda_1^*, \lambda_2^*) \\ &= H_{hys}^{-1}\Big(\frac{B_a}{\mu_0 N}(4x_g + \frac{l_{m1}}{\mu_r}), \lambda_1^*, \lambda_2^*\Big) \end{aligned} \tag{2.69}$$

where $\lambda_1^* = \frac{l_{m1}}{N}\lambda_1$ and $\lambda_2^* = \frac{1}{(4x_g\mu_r + l_{m1})}\lambda_2$. From Equation (2.69), we get:

$$B_a = \frac{\mu_0 N}{(6x_g + \frac{l_{m1}}{\mu_r})} \cdot H_{hys}(i, \lambda_1^*, \lambda_2^*). \tag{2.70}$$

In the iron, $\mu_r \gg 1$, so the magnetization of the iron is often neglected. In this case, Equation 2.70 may be simplified to:

$$B_a = \frac{\mu_0 N}{6x_g} \cdot H_{hys}(i, \lambda_1^*, \lambda_2^*). \tag{2.71}$$

When $b = 2a$ as shown in Figure 2.5:
By substituting Equation (2.9), Equation (2.55) can be rewritten as:

$$i = \frac{4x_g}{\mu_0 N} \cdot B_a + \frac{l_{m2}}{N} \cdot H_{hys}^{-1}(\frac{B_a}{\mu_0\mu_r}, \lambda_1, \lambda_2). \tag{2.72}$$

Splitting the hysteresis operator in Equation (2.72) as in Equation (2.5) yields

$$i = \frac{B_a}{\mu_0 N}(4x_g + \frac{l_{m2}}{\mu_r}) + \frac{l_{m2}}{N} \cdot \varphi(\frac{B_a}{\mu_0\mu_r}, \lambda_1, \lambda_2). \tag{2.73}$$

After applying Proposition 1.6, Equation (2.73) becomes

$$\begin{aligned} i &= \frac{B_a}{\mu_0 N}(4x_g + \frac{l_{m2}}{\mu_r}) + \varphi\Big(\frac{B_a}{\mu_0 N}(4x_g + \frac{l_{m2}}{\mu_r}), \lambda_1^*, \lambda_2^*\Big) \\ &= H_{hys}^{-1}\Big(\frac{B_a}{\mu_0 N}(4x_g + \frac{l_{m2}}{\mu_r}), \lambda_1^*, \lambda_2^*\Big) \end{aligned} \tag{2.74}$$

where $\lambda_1^* = \frac{l_{m2}}{N}\lambda_1$ and $\lambda_2^* = \frac{1}{(4x_g\mu_r + l_{m2})}\lambda_2$. From Equation (2.74), we get:

$$B_a = \frac{\mu_0 N}{(4x_g + \frac{l_{m2}}{\mu_r})} \cdot H_{hys}(i, \lambda_1^*, \lambda_2^*). \tag{2.75}$$

In the iron, $\mu_r \gg 1$, so the magnetization of the iron is often neglected. In this case, Equation (2.70) may be simplified to:

$$B_a = \frac{\mu_0 N}{4x_g} \cdot H_{hys}(i, \lambda_1^*, \lambda_2^*). \tag{2.76}$$

2.4.6 Magnetic force with hysteresis

When $b = a$ as shown in Figure 2.5:
From Equation (2.70) and (2.61), we get:

$$F = 3N^2\mu_0 A_a \frac{(H_{hys}(i, \lambda_1^*, \lambda_2^*))^2}{(\frac{l_{m1}}{\mu_r} + 6x_g)^2}. \tag{2.77}$$

Neglecting the Iron
From Equation (2.71) and (2.61), we get:

$$F = \frac{1}{12}N^2\mu_0 A_a \frac{(H_{hys}(i, \lambda_1^*, \lambda_2^*))^2}{x_g^2}. \tag{2.78}$$

When $b = 2a$ as shown in Figure 2.5:
From Equation (2.70) and (2.64), we get:

$$F = 2N^2\mu_0 A_a \frac{(H_{hys}(i, \lambda_1^*, \lambda_2^*))^2}{(\frac{l_{m2}}{\mu_r} + 4x_g)^2}. \tag{2.79}$$

Neglecting the Iron
From Equation (2.76) and (2.64), we get:

$$\begin{aligned} F &= \frac{1}{8}N^2\mu_0 A_a \frac{(H_{hys}(i, \lambda_1^*, \lambda_2^*))^2}{x_g^2} \\ &= \eta \frac{(H_{hys}(i, \lambda_1^*, \lambda_2^*))^2}{x_g^2} \end{aligned} \tag{2.80}$$

This model contains both the hysteresis and obvious square linearity between the input and output. If the reluctance actuator is modeled by Equation (2.80), the curves of input current and the corresponding output force are obtained as shown in Figure 2.8. It can be seen that the hysteresis model Equation (2.80) provides a good approximation for the hysteresis phenomenon between the input current i and output force F.

2.5 Conclusion

The reluctance linear actuator models are discussed in this chapter. The parametric hysteresis operator is reviewed firstly. Further, the models without hysteresis for reluctance linear actuator with C-core and E-core are reviewed; the

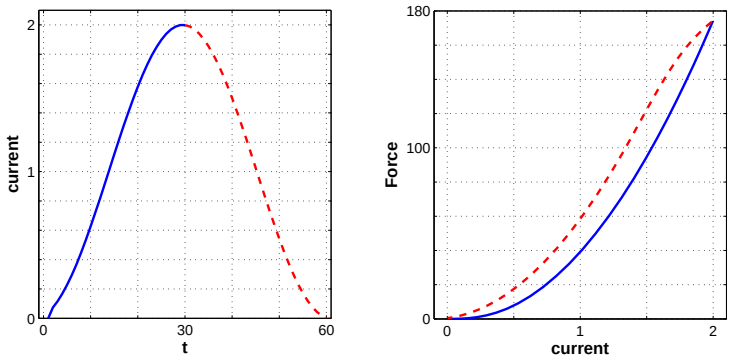

Figure 2.8: Curve of an input current and the corresponding output force based on the current-driven reluctance actuator model with hysteresis

models with hysteresis for reluctance linear actuator with C-core and E-core are proposed.

3

Nonlinear Control for Reluctance Linear Actuator

3.1 Introduction

In this chapter, the basic control method and nonlinear current control for reluctance actuator are reviewed.

3.2 Control of reluctance linear actuator

3.2.1 Nonlinear current compensation

A typical structure of the current-driven reluctance linear actuator control is shown in Figure 3.1. Due to the unstable nature of the electromagnetic forces,

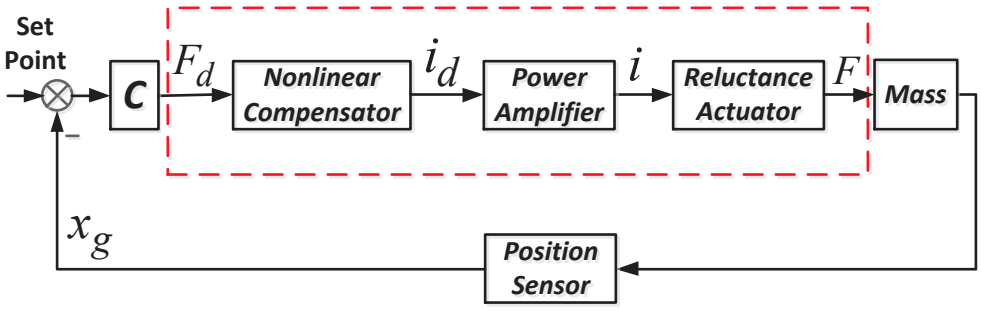

Figure 3.1: Typical current-driven reluctance actuator control loop.

a feedback control loop is required to achieve stable performance. In Figure 3.1, "C"denotes a linear position controller such as the proportional-integral-derivative (PID) controller, which guarantees the stability of the closed loop. The position controller uses the position in the air gap measured by a position sensor to generate the force command F_d. The power amplifier supplies the current for the reluctance actuator.

From Equation (2.24), a nonlinear current compensator can be obtained [80] as

$$i_d = \sqrt{\frac{F_d \cdot x_g^2}{\eta_d}} \tag{3.1}$$

where η_d is the estimate of real constant η.

The above nonlinear current compensator does not consider the hysteresis in the reluctance force. From the analysis of the hysteresis influence in the introduction, it is necessary to find a hysteresis compensation method for the reluctance linear actuator in the high-precision positioning.

3.2.2 Control of a stage having paired reluctance linear actuator

Usually, six motion directions of the fine stage in a lithographic tool are defined in a coordinate system [8] and six separate single-input single output controller can be decoupled for each motion direction. In this section, only one motion direction is considered, such as the scanning direction. The fine stage is supported vertically by anti-friction bearings such as air bearings. The size of the wafer stage is corresponding to the circular wafer having a diameter of 200, 300, or 450 mm. Due to the nature of reluctance force, an E/I core actuator can only generate a unidirectional attractive force. To generate an active force in the opposite direction, a second actuator needs to be placed on the opposite side. Figure 3.2 illustrates a simplified one motion direction fine stage [80] having paired reluctance actuators E-core 1 and E-core 2. The material of fine stage is the carbon fiber to reduce the weight for the higher acceleration. The material of the E-core and the I-target is the Cobalt-Iron.

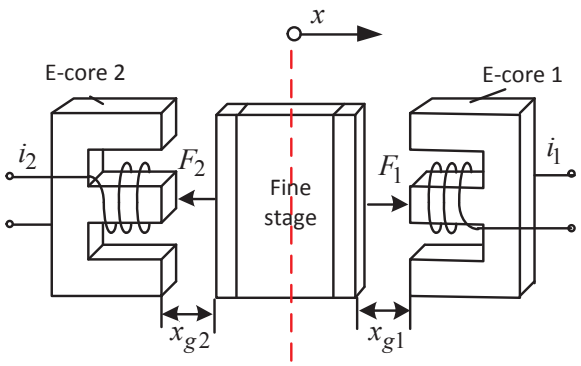

Figure 3.2: Paired E/I core actuator.

The gaps between the E-core 1,2 and the stage are x_{g1} and x_{g2}, which can be measured by suitable sensors such as capacitor sensor. The force F_1 and F_2 are nonnegative, while the difference between F_1 and F_2 can take any value and direction. In the initial state, the gaps are $x_{g1} = x_{g0}$ and $x_{g2} = x_{g0}$, where x_{g0} is the initial gap. In Figure 3.2, we define the right as the positive direction. Furthermore, when the stage moves to the positive direction, the gaps become $x_{g1} = x_{g0} - x$ and $x_{g2} = x_{g0} + x$ respectively where x is the global placement and can be measured by position sensor such as a laser interferometer [80].

A conventional control scheme is depicted in Figure 3.3, in which the controller $C(s)$ is formed by a proportional-integral-derivative (PID) controller, a lowpass filte and a lead compensatorr. In the feedback loop, the controller uses the position of the stage measured by a position sensor to generate the applied force command. The filter $Q(s)$ generates a feedforward force based on the setpoint position. When $P(s)$ is described by $1/ms^2$, $Q(s) = ms^2$ generats a force that is proportional to the setpoint acceleration.

The final position accuracy is determined by measurement system errors, disturbance forces including the nonlinearity force caused by the hysteresis, which have an effect on the closed loop performance. Rejection of output (measurement) disturbances and input (force) disturbances is judged by, respectively, the

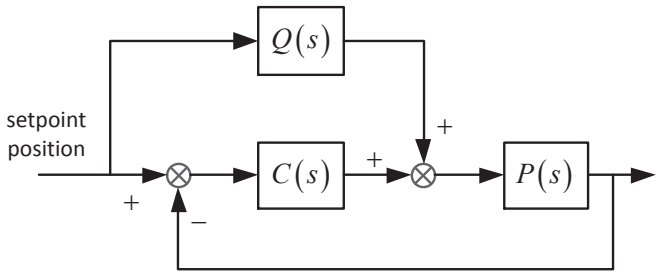

Figure 3.3: Basic control scheme.

output sensitivity

$$G_{os} = \frac{1}{1 + P(s)C(s)} \tag{3.2}$$

and the process sensitivity

$$G_{ps} = \frac{P(s)}{1 + P(s)C(s)}. \tag{3.3}$$

Based on the conventional controller shown in Figure 3.3, a control loop for the fine stage having paired E/I core actuator is shown in Figure 3.4. $G_s(s)$ denotes the position controller, $Q_s(s)$ denotes the feedforward controller, $P_s(s)$ denotes the fine stage process, "EI1"and "EI2"denote the E-core 1 and E-core2, "NC1"and "NC2"denote nonlinear current compensator and "FD"denotes the force distribution.

In Figure 3.4, "FD"distributes the desired force to each E/I core actuator as follows:

$$F_{d1}{=}F_0 + F_d/2, \tag{3.4}$$

$$F_{d2}{=}F_0 - F_d/2 \tag{3.5}$$

where F_0 is the bias force generated by paired E/I core actuator respectively in the opposite direction, which provides a zero net force on the stage, thus maintaining the position of the stage. In this chapter, F_0 is determined as $F_0 = F_{max}/2$, in which F_{max} is the maximum force corresponding the maximum acceleration. More details about how to select the bias force F_0 can be found in patent [12].

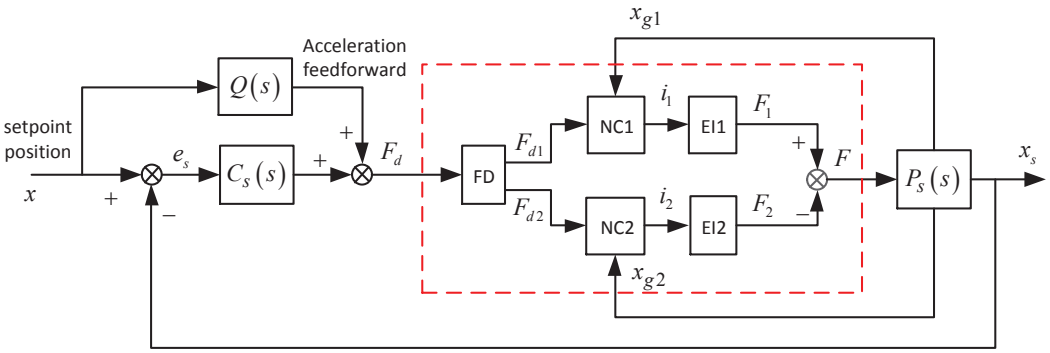

Figure 3.4: Paired E/I core actuator control.

Since there exits strong linearity between the input current i and output force F, from Equation (3.1), nonlinear current compensators "NC1"and "NC2"can be obtained as

$$i_1 = \sqrt{\frac{F_{d1} \cdot x_{g1}^2}{\eta_d}}, \tag{3.6}$$

$$i_2 = \sqrt{\frac{F_{d2} \cdot x_{g2}^2}{\eta_d}}, \tag{3.7}$$

where η_d is the estimate of real constant η. However, the reluctance actuator use the soft magnet material, which has a hysteresis between the input current i and output force F in reluctance actuators "EI1"and "EI2"as shown in Figure 3.4. Since the nonlinear current compensators "NC1"and "NC2"can not compensate the hysteresis between the input current i and output force F in each E/I actuator, a hysteresis force results in between the position controller force command F_d and the real output force F. However, the hysteresis influence must be considered in the high-precision positioning [39], so it is necessary to find a hysteresis compensation method for the reluctance linear actuator.

3.3 Conclusion

In this chapter, the basic control method and nonlinear current control for reluctance actuator are reviewed.

4

Hysteresis Compensation for a Current-driven Reluctance Linear Actuator Using Adaptive MNN

4.1 Introduction

A variety of models and compensation algorithms have been developed for the hysteresis [36][32][1][87]. The classical approach is to construct a hysteresis inverse and use it as a feed-forward compensator [32] together with a feedback control. The hysteresis compensation method via Preisach model inversion has been proposed in [55]. An inverse parametric hysteresis model [39] was used in current-mode operated reluctance force actuator. However, the above methods need precise hysteresis model, which is usually complex and hard to obtain.

Owing to the online self-learning and estimation capability of the neural network, it provides a good solution for solving nonlinear problems. Especially, the multi-layer neural network (MNN) is effectively used in nonlinear discrete-time system identification and control [49]. Although a lot of researches have been done on the neural network application to the hysteresis [61] [20], the neural network compensation for the current-driven reluctance actuator with hysteresis has yet to be studied.

The main contributions of this section is a hysteresis compensator for current-driven reluctance linear actuator using the adaptive MNN proposed for the first

time. Concretely speaking, based on the input-output feature of the hysteresis in reluctance force and the learning and approximation ability of neural network, a hysteresis current compensator is proposed for the current-driven reluctance actuator with hysteresis using the adaptive MNN [49], whose weight is updated by the error between the desired force and the actual force. The main advantage of the proposed compensation method is that the inverse hysteresis model does not be required. Simulations are conducted on the reluctance actuator model with hysteresis and the results show that the adaptive MNN is effective in overcoming the hysteresis and promising in high precision and high acceleration control applications.

4.2 Neural network

Since McCulloch and Pitts [62] introduced the idea of studying the computational abilities of networks composed of simple models of neurons in the 1940s, neural network techniques have been successfully applied in many fields such as learning, pattern recognition, signal processing, modelling and system control. The approximation abilities of neural networks have been proven in many research works [15][22][13][71][31]. The early works on neural network applications to controller design were reasearched in [86][2][69][35][64]. In the late 1980s, the popularization of backpropagation (BP) algorithm [70] greatly boosted the development of neural control and many neural control approaches have been developed [60][59]. The analytical results obtained in [21][46] showed that using multi-layer neural networks as function approximators could guarantee the stability of the systems when the initial network weights chosen were sufficiently close to the ideal weights.

Recently, neural networks have been made particularly attractive and promising for applications to modelling and control of nonlinear systems. For neural network controller design of general nonlinear systems, several researchers have suggested to use neural networks as emulators of inverse systems. Using the implicit function theory, the NN control methods proposed in [28] [46] have been used to emulate the "inverse controller" to achieve the desired control objectives. Based on this idea, an adaptive controller has been developed using high order

neural networks with stable internal dynamics in [90] and applied in [25]. As an alternative, neural networks have been used to approximate the implicit desired feedback controller in [24].

In nonlinear system control, neural networks can be applied as a function approximators to emulate the "inverse" control. For example, neural networks combined backstepping design are reported in [27][85], using neural networks to construct observers can be found in [57][16], neural network control in robot manipulators are reported in [76][81][82], neural control for distillation column are reported in [72].

HONN(high order neural networks), RBF(Radial basis function neural networks) and MNN(multi-layer neural network) are three kinds of frequently used neural networks in nonlinear system control and identification[85][3]. HONN and RBF networks can be considered as two-layer networks, in which the input space is mapped on to a new space. The output layer combines the outputs in the latter space linearly. MNN is a static feed-forward network that consists of a number of layers, each layer having a number of McCulloch-Pitts neurons [62]. Due to its hidden layers, the MNN has an important character that it can approximate any continuous nonlinear function. Once the hidden layers have been selected, only the adjustable weights have to be determined to specify the networks completely. Since each node of any layer is connected to all the nodes of the following layer, it follows that a change in a single parameter at any one layer will generally affect all the outputs in the following layers. MNNs with one or more hidden layers are capable of approximating any continuous nonlinear function, which was shown independently by [22][13][71]. This important character makes it one of the most widely used neural networks in system modelling and control.

In this thesis, the MNN will be used to compensate the hysteresis in the reluctance linear actuator.

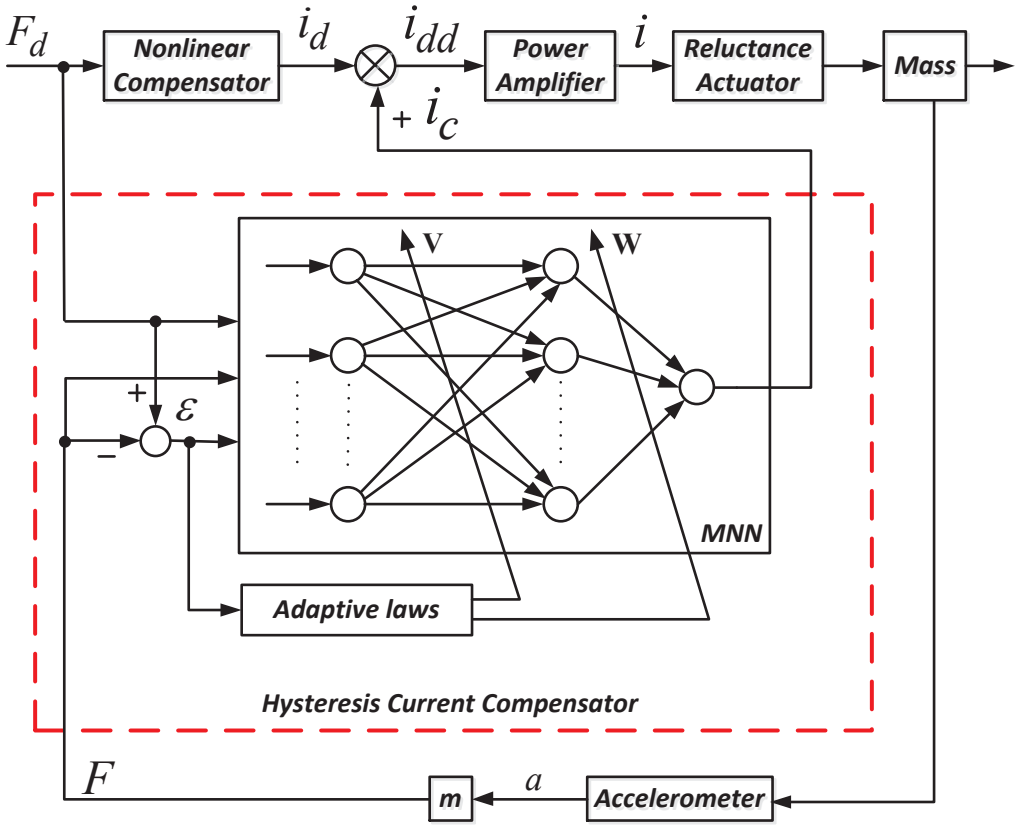

Figure 4.1: Structure of hysteresis current compensator using adaptive MNN.

4.3 Design of nonlinear current compensator using adaptive MNN

A typical structure of the current-driven reluctance linear actuator control is shown in Figure 3.1. Due to the unstable nature of the electromagnetic forces, a feedback control loop is required to achieve stable performance.

The nonlinear current compensator (3.1) does not consider the hysteresis in the reluctance force. From the analysis of the hysteresis influence in introduction, it is necessary to find a hysteresis compensation method for the reluctance linear actuator in the high-precision positioning. In the following, a hysteresis compensator for the reluctance linear actuator based on the adaptive MNN will

be apposed.

Owing to the advantages of MNN, a hysteresis current compensator using the adaptive MNN can be obtained as shown in Figure 4.1 for the current-driven reluctance actuator force. The feedback force F can be estimated from the relation $F = ma$, with m being the stage mass and a the actual acceleration. The actual acceleration a can be measured by an accelerometer or computed from the measured gap position x_g by a digital double differentiator. The double differentiation may introduce a noise. However, when a filter such as the least-square method and considering the noise level makes double differentiation acceptable as a method to calculate the stage acceleration [9]. In this section, the acceleration a is assumed to be measured by the accelerometer. The detail of the adaptive MNN is as follows.

The current command $i_d(k)$ is compensated by the output $i_c(k)$ of the adaptive MNN

$$i_{dd}(k) = i_d(k) + i_c(k). \tag{4.1}$$

At instant k, the nonlinear term $i_c(k)$ in Equation (4.1) is estimated by the following MNN

$$i_c(k) = \mathbf{W^T(k)S(V^T(k)\bar{x}(k))}. \tag{4.2}$$

Here, $\mathbf{W(k)} \in \mathbf{R^{l+1}}$ and $\mathbf{V(k)} \in \mathbf{R^{(2n+1)\times l}}$ are weighting matrices, l is the number of hidden-layer neurons, $\bar{\mathbf{x}}(k) = [\mathbf{x}^T(k), 1]^T$ denotes the input vector of the neural network, $\mathbf{x}^T(k) = [F_d(k+1), F_d(k), F(k+1), F(k)]$, and $\mathbf{S(V^T(k)\bar{x}(k))} = [\mathbf{s(v_1^T(k)\bar{x}(k))}, \cdots, \mathbf{s(v_l^T(k)\bar{x}(k))}, \mathbf{1}]^\mathbf{T}$ with $s(x) = 1/(1+e^{-x})$.

The MNN estimation error is

$$\varepsilon(k+1) = F_d(k) - F(k). \tag{4.3}$$

The adaptive update law of the neural network weight is chosen as

$$\mathbf{W}(k+1) = \mathbf{W}(k) - \mathrm{Proj}_W[\gamma_w \mathbf{S}(k)\varepsilon(k+1)] \tag{4.4}$$

$$\mathbf{V}(k+1) = \mathbf{V}(k) - \mathrm{Proj}_\mathbf{V}[\gamma_v \mathbf{z}_l \mathbf{W}^T(k)\mathbf{S}'(t)\varepsilon(k+1)] \tag{4.5}$$

where γ_w and γ_v are the learning rates with positive constants, $\mathbf{S}(k) = \text{diag}\{s_1(k), \cdots, s_l(k)\}$ with $s_i(k) = s(v_i^T \bar{\mathbf{x}}(k))$, $\mathbf{z}_l = [1/\sqrt{l}, \cdots, 1/\sqrt{l}]^T (\|\mathbf{z}\| = 1)$ is a vector compatible with $\mathbf{V}(k)$. $\mathbf{S}'(k) = \text{diag}\{s_1'(k), \cdots, s_l'(k)\}$ is a diagonal matrix with $s_i'(k) = s'(v_i^T \bar{\mathbf{x}}(k))$. Since the output of the hidden layer neural network is directly related to the input of the output weight, the output weight is introduced in Equation 4.5. The projection function $\text{Proj}_\theta(*)$ is defined as $\text{Proj}_\theta(*) = \{\text{Proj}_\theta(*_{jk})\}$ whose element in the j-th row and k-th column is:

$$\text{Proj}_\theta(*_{\text{jk}}) = \begin{pmatrix} -*_{jk} & \begin{pmatrix} \theta_{jk} = \rho_{\theta_{jk},\max} \text{ and } *_{jk} < 0 \\ \theta_{jk} = \rho_{\theta_{jk},\min} \text{ and } *_{jk} > 0, \end{pmatrix} \\ {}_{jk} & \text{otherwise} \end{pmatrix} \tag{4.6}$$

where $*$ is either a vector or matrix with its element being $*_{jk}$, $\rho_{\theta_{jk},\min}$ and $\rho_{\theta_{jk},\max}$ are presumed upper and lower bound of θ_{ij}, and θ denotes $\mathbf{W}$ and $\mathbf{V}$. However, due to the fact that those bounds may not be known a priori, certain fictitious large enough bounds can be used [29]. We just need to limit the output amplitude of the output of adaptive MNN (4.1), e.g. limit the power amplifier input within ± 10 v.

4.4 Simulations

Example 1: A simulation for the current-driven reluctance actuator is conducted to verify the performance of the proposed hysteresis compensation configuration shown in Figure 4.1.

Items	Values
the maximum force	200 N
the maximum gap x_g	0.4 mm
the E/I constant	$k = 7.73 \times 10^{-6}$

Table 4.1: E/I core parameters.

In this simulation, since the linear power amplifier has a high bandwidth and rapid response, it is ignored. When a force command F_d is imposed without a counter balance force, the I-target would be pulled to the E-core. For this reason, it is assumed that the I-target is fixed, so that we may investigate the force

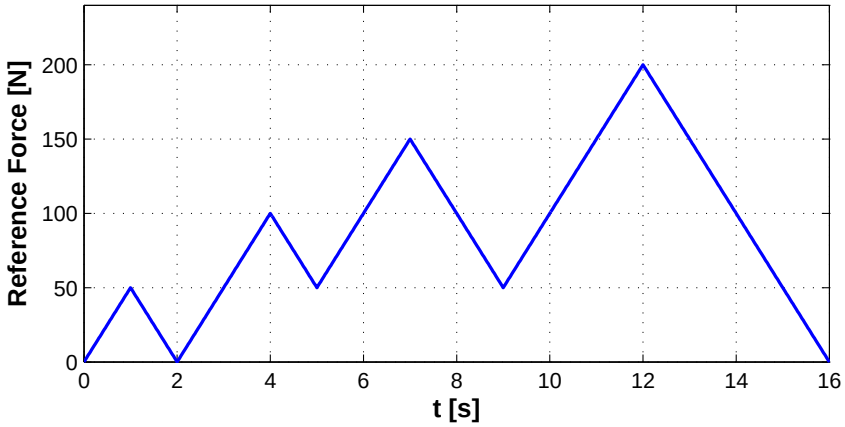

Figure 4.2: Reference force.

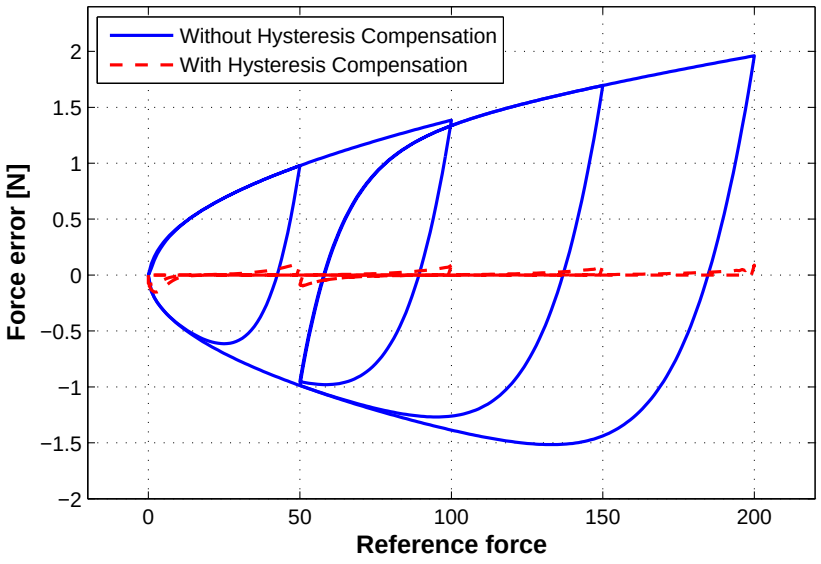

Figure 4.3: Comparison of the force error between force generations without hysteresis compensation and with hysteresis compensation.

tracking performance. The reluctance linear actuator with hysteresis is modeled by Equation (2.80), whose parameters chosen as in the patent [12] as shown in table (4.1):

To reproduce a reluctance actuator model with non-smooth hysteresis, the parameter λ_2 of the hysteretic operator Equation (2.80) would have to be infinitely large. Here, the hysteresis operator parameters are chosen as $\lambda_1 = 0.02$ and $\lambda_2 = 10$.

The control objective is to make the system output F following the reference force F_d. A non-trivial reference force depicted in Figure 4.2. This profile is used to test the proposed nonlinear controller with hysteresis compensation with respect to higher order reversal curves. The adaptive MNN compensator (4.1) is designed to compensate the hysteresis. The parameters of the adaptive MNN are determined as: the input vector of the neural network is chosen as $\mathbf{x}(k) = [F_d(k+1), F_d(k), F(k+1), F(k)]$, the number of hidden-layer neurons is $l = 40$, the initial neural network weighting matrices are $\mathbf{w}(\mathbf{0}) = \mathbf{0}$ and $\mathbf{v}(\mathbf{0}) = \mathbf{0}$, the learning rate are selected as $\gamma_w = 0.0006$ and $\gamma_v = 0.01$ respectively.

The maps between the reference force $F_d(k)$ and the output force $F(k)$ tracking error with nonlinear current control without hysteresis compensation and with hysteresis compensation are shown in Figure 4.3. The largest force tracking error without hysteresis compensation is about ± 2 N. With hysteresis compensation, it is about ± 0.1 N. Furthermore, Figure 4.4 shows that the ratio between the output force $F(k)$ and its reference command $F_d(k)$ with and without hysteresis compensator, and the ratio with hysteresis compensation is very close to 1 with compensation. From the simulation results, it is clear that the force with hysteresis compensation has a much smaller force tracking error than without hysteresis compensation.

Example 2: In order to verify if the proposed hysteresis compensation method can be applied in high-precision systems, we do the following simulation using the reluctance actuator to drive a one degree of freedom stage.

Due to the nature of the reluctance force, an E/I core actuator can only generate a unidirectional attractive force. To generate an active force in the opposite direction, a second actuator needs to be placed on the opposite side of the I-Target as shown in Figure 3.2, in which including electromagnetic actuators

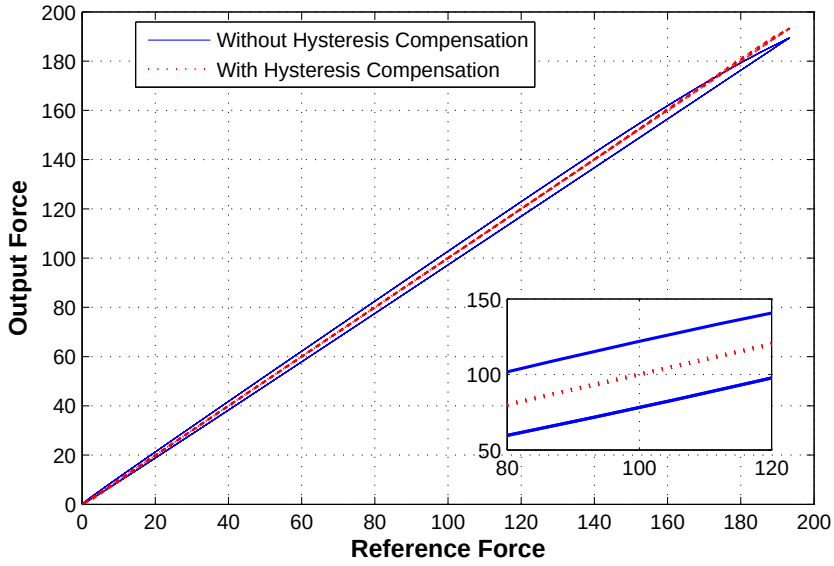

Figure 4.4: Comparison of the force hysteresis loop between force generations without hysteresis compensation and with hysteresis compensation.

E-core 1 and E-core 2 as well as a stage [12]. Choose Equation (2.80) as the E/I core actuator model with hysteresis. The gap x_{g1} separates the E-core 1 and the I-target 1 and the gap x_{g2} separates E-core 2 and I-target 2. The stage parameters are shown in table (4.2)

Items	Values
the stage mass	10 kg
the position sensor resolution	1 nm
the sampling time	$0.5ms$
the bias force	$F_0 = 15\ N$
The E-core electromagnetic constant	$k = 7.73 \times 10^{-6}$

Table 4.2: E/I stage simulation parameters.

The gap x_{g1} and x_{g2} between the E-core 1,2 and the I-target1,2 are in the range of 0 μm to 400 μm and the initial gap is $x_{g0} = 400\ \mu m$. The parameters of hysteresis operator are set as in Example 1.

The stage control system uses the proportional-integral (PI) controller to guar-

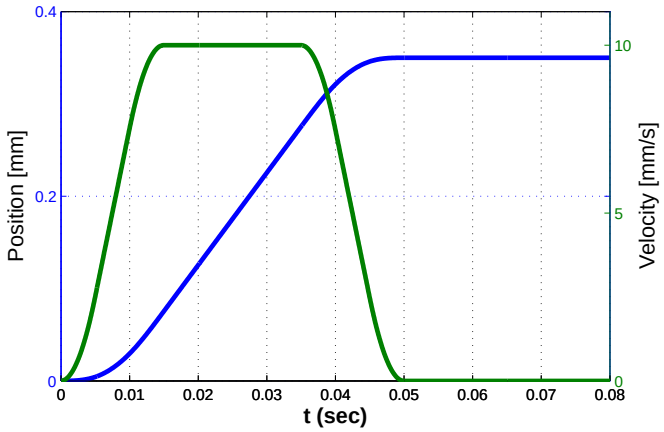

Figure 4.5: Reference position and velocity.

antee the stability of the closed-loop position system, while the adaptive MNN hysteresis compensator is employed to reduce the influence of the hysteresis and improve the performance of the closed-loop position system. The adaptive MNN parameters for the two E/I actuators are the same as Example 1.

The control objective is to make the stage position x follow the reference position. The reference trajectory is determined by the 3rd order trajectory planning method [43]. The position and velocity are shown in Figure 4.5. The trajectory values are shown in table (4.3).

Items	Values
the largest displacement	350 μm
the maximum velocity	10 mm/s
the maximum acceleration	1 m/s^2
the jerk	200 m/s^3

Table 4.3: Trajectory values.

The position tracking errors of control without hysteresis compensation and with hysteresis compensation are shown in Figure 4.6. We define the constant velocity settling time and the stop time as the time instants after which the position tracking error is less than 1 μm. From the enlarged view of the constant velocity segment shown in Figure 4.7, it can be seen that the constant veloc-

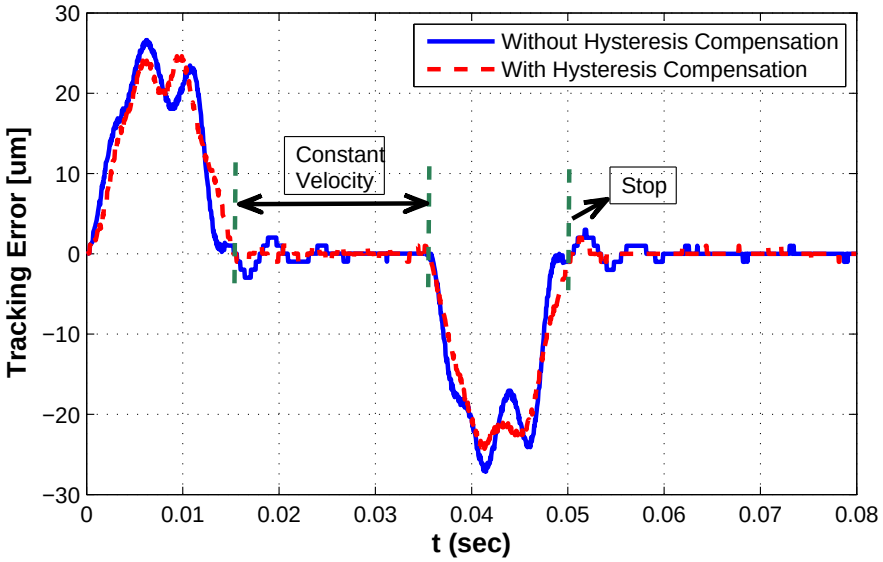

Figure 4.6: Comparison of the position tracking error between controls without hysteresis compensation and with hysteresis compensation.

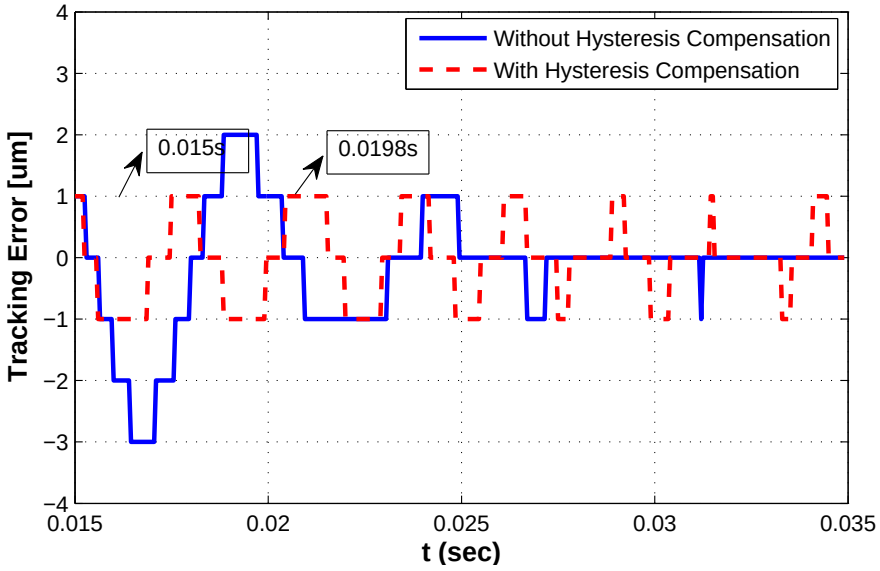

Figure 4.7: Comparison of the position tracking error between controls without hysteresis compensation and with hysteresis compensation in the constant velocity segment.

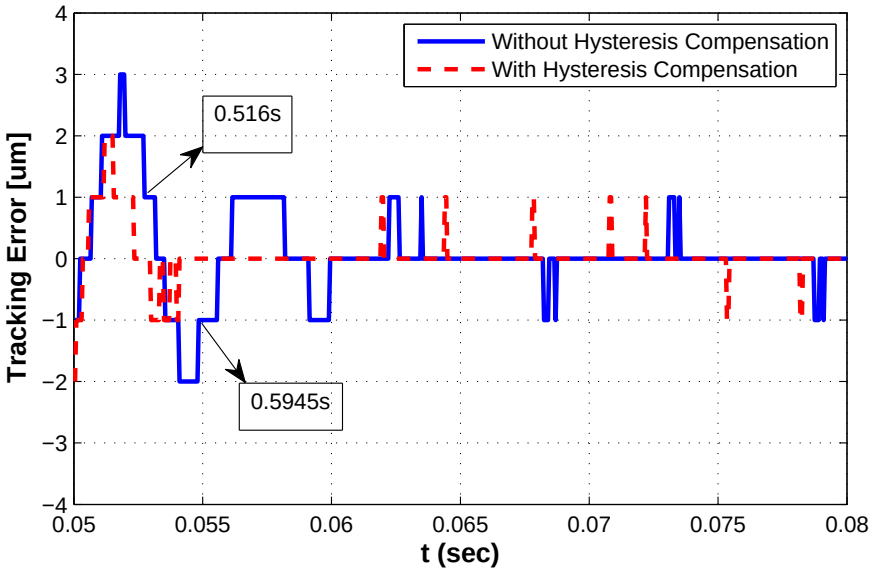

Figure 4.8: Comparison of the position tracking error between controls without hysteresis compensation and with hysteresis compensation in the stop segment.

ity settling time without hysteresis compensation (0.0198 s) is about 1.32 times longer than with hysteresis compensation (0.015 s), and from the enlarged view of the stop segment shown in Figure 4.8, the stop time without hysteresis compensation (0.5945 s) is about 1.1521 times longer than with hysteresis compensation (0.516 s).

From the simulation results of the one degree E/I stage, it is verified that the adaptive MNN hysteresis compensator provides a feasible solution to reduce the influence of reluctance actuator with hysteresis.

4.5 Conclusion

A hysteresis compensation control configuration has been proposed for the reluctance actuator using the discrete-time adaptive MNN, which is used as a hysteresis learning machine of nonlinearity. The proposed hysteresis compensator compensates the current based on the desired force and the actual force using the adaptive MNN. This hysteresis compensator does not need the inverse hysteresis model. Due to the simplicity of the compensation configuration, it may have a

wider range of applications. Simulation results show that the proposed methods are effective in overcoming the hysteresis and promising in high-precision control applications.

4. HYSTERESIS COMPENSATION FOR A CURRENT-DRIVEN RELUCTANCE LINEAR ACTUATOR USING ADAPTIVE MNN

5

A Direct Adaptive MNN Control Method for Stage Having Paired Reluctance Linear Actuator with Hysteresis

5.1 Introduction

As has been stated in the previous chapter, owing to its online self-learning ability, the neural network provides a good solution for solving nonlinear problems. Especially, the multi-layer neural network (MNN) is effectively used in nonlinear discrete-time system identification and control [49] [26]. Although a lot of researches have been done on the neural network application to the hysteresis [61] [20], there is few hysteresis compensation algorithms for the reluctance actuator from the available information. A hysteresis compensation configuration for the current-driven reluctance actuator with hysteresis using adaptive MNN has been proposed in paper [89] by the authors in **Chapter** 4, but this method has to use the reluctance actuator model.

In this chapter, a new and direct adaptive MNN [47] controller is proposed for the current-driven reluctance linear actuator with hysteresis. The main advantage of the proposed adaptive MNN controller is that the reluctance linear actuator

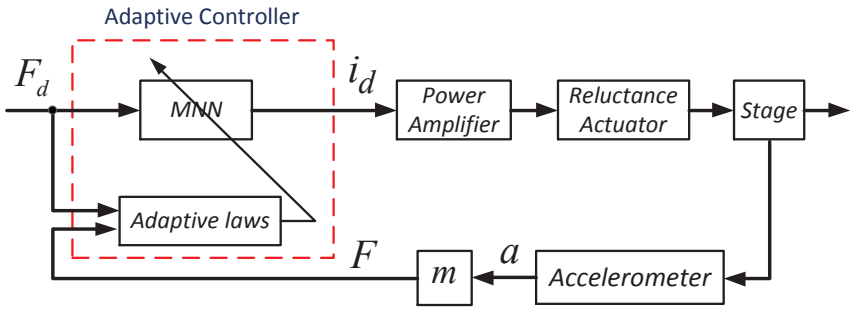

Figure 5.1: Direct adaptive MNN control for reluctance linear actuator.

model and the inverse hysteresis model are not required. Then, a control configuration is proposed for stages having paired E/I core actuator with hysteresis using the proposed adaptive MNN controller. Simulations are conducted on a stage having paired reluctance actuator with hysteresis and the results show that the adaptive MNN controller is effective in overcoming the nonlinearity and parameter uncertainty of the reluctance linear actuator.

5.2 Direct adaptive MNN control for reluctance linear actuator

5.2.1 Nonlinear control using adaptive neural network

Figure 3.1 shows a typical feedback control loop for a current-driven reluctance linear actuator, but the current compensator (3.1) does not consider the hysteresis in the reluctance force and is highly sensitive to the parameter η_d. However, hysteresis effect must be considered for high-precision motion control. In the following, a direct hysteresis compensator for the reluctance actuator based on the adaptive MNN is proposed.

A nonlinear controller using the adaptive MNN [26] for the current-driven reluctance actuator is proposed as shown in Figure 5.1. This structure state the difference from Chapter 4 treats the nonlinearity between the force command F_d and the output force F directly and overcomes the robustness issue with respect to parameter uncertainty. The feedback force F can be estimated from the relation $F = ma$, with m the stage mass and a the actual acceleration. The acceleration a

is measured by the accelerometer. The detail of the adaptive MNN is as follows. At instant k, the command current $i_d(k)$ is given by:

$$i_d(k) = \mathbf{W}^T(k)\xi(\mathbf{V}^T(k)\bar{\mathbf{p}}(\mathbf{k})) \tag{5.1}$$

where $\mathbf{W}(t) = [w_1, \cdots, w_{l+1}] \in \mathbf{R^{l+1}}$ and $\mathbf{V}(t) = [v_1, \cdots, v_l] \in \mathbf{R^{(n+1)\times l}}$ are weighting matrices, l is the number of hidden-layer neurons, select $\mathbf{p}(k) = [F_d(k+1), F_d(k), F(k+1), F(k)]$, then $\bar{\mathbf{p}}(k) = [\mathbf{p}(k), 1]^T$ denotes the neural network input, $\xi(\mathbf{V}^T\bar{\mathbf{p}}(k)) = [\xi(v_1^T\bar{\mathbf{p}}(k)), \cdots, \xi(v_l^T\bar{\mathbf{p}}(k)), 1]^T$ with $\xi(p) = 1/(1+e^{-p})$. The force tracking error is:

$$\varepsilon(k+1) = F_d(k) - F(k). \tag{5.2}$$

The neural network weights are updated online based on the adaptive laws using the force tracking error Equation (5.2). The adaptive update laws are chosen as

$$\mathbf{W}(k+1) = \mathbf{W}(k) - \mathrm{Proj}_{\hat{W}}[\Gamma_w\xi(k)\varepsilon(k+1)], \tag{5.3}$$

$$\mathbf{V}(k+1) = \mathbf{V}(k) - \mathrm{Proj}_{\mathbf{V}}[\Gamma_v\mathbf{z}_l\mathbf{W}^T(k)\xi'(k)\varepsilon(k+1)] \tag{5.4}$$

where γ_w and γ_v are the positive learning rates, $\xi(k) = \mathrm{diag}\{\xi_1(k), \cdots, \xi_l(k)\}$ with $\xi_i(k) = \xi(v_i^T\bar{\mathbf{p}}(k))$, $\mathbf{z}_l = [1/\sqrt{l}, \cdots, 1/\sqrt{l}]^T$ ($\|\mathbf{z}\| = 1$) is a vector compatible with $\mathbf{V}(k)$. $\xi'(k) = \mathrm{diag}\{\xi_1'(k), \cdots, \xi_l'(k)\}$ is a diagonal matrix with $\xi_1'(k) = \xi'(v_i^T\bar{\mathbf{p}}(k))$. Since the output of the hidden layer neural network is directly related to the input of the output weight, so the output weight $\mathbf{W}$ is introduced in Equation 5.4. Define the projection function as $\mathrm{Proj}_\theta(*) = \{\mathrm{Proj}_\theta(*_{jk})\}$, whose element in the j-th row and k-th column is:

$$\mathrm{Proj}_\theta(*_{\mathrm{jk}}) = \begin{pmatrix} -*_{jk} & \begin{pmatrix} \theta_{jk} = \rho_{\theta_{jk},\max} \text{ and } *_{jk} < 0 \\ \theta_{jk} = \rho_{\theta_{jk},\min} \text{ and } *_{jk} > 0, \end{pmatrix} \\ {}_{jk} & \text{otherwise} \end{pmatrix} \tag{5.5}$$

where $*$ is either a vector or matrix with its element being $*_{jk}$, $\rho_{\theta_{jk},\min}$ and $\rho_{\theta_{jk},\max}$ are presumed upper and lower boundaries of θ_{ij}, and θ denotes $\mathbf{W}$ and $\mathbf{V}$.

5.2.2 Application to 1-DOF stage having paired reluctance linear actuator

Due to the nature of reluctance force, an E/I core actuator can only generate a unidirectional attractive force. To generate an active force in the opposite

5. A DIRECT ADAPTIVE MNN CONTROL METHOD FOR STAGE HAVING PAIRED RELUCTANCE LINEAR ACTUATOR WITH HYSTERESIS

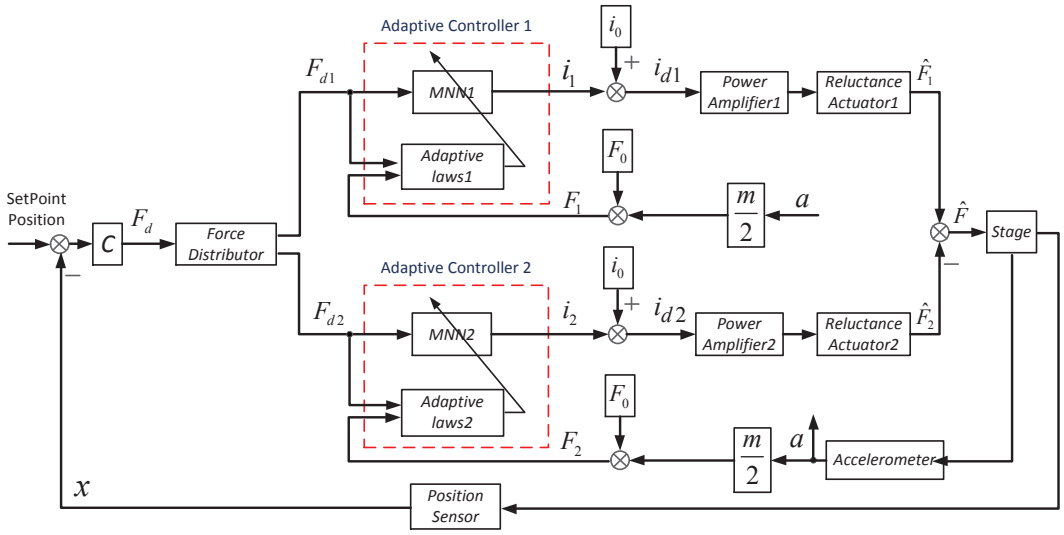

Figure 5.2: Nonlinear control structure for stage having paired E/I core actuator using adaptive MNN.

direction, a second actuator needs to be placed on the opposite side. A control loop for one-degree-of-freedom stage having paired E/I core actuator as shown in Figure 3.2 using adaptive MNN is shown in Figure 5.2. Since two reluctance actuators are used, we need two adaptive MNN controllers to compute the desired current for each of them.

In Figure 5.2, the controller "C "uses the position error between the set-point and the measured position to determine the desired force F_d which should be exerted to reach desired stage position. The force distributor distributes the desired force to each E/I actuator as follows:

$$F_{d1}=F_0 + F_d/2, \tag{5.6}$$

$$F_{d2}=F_0 - F_d/2 \tag{5.7}$$

where F_0 is the bias force generated by paired E/I actuator respectively in the opposite direction, which provides a zero net force on the stage, thus maintaining the position of the stage. In this paper, F_0 is determined as $F_0 = F_{max}/2$, in which F_{max} is the maximum force corresponding the maximum acceleration. More details about how to select the bias force F_0 can be found in patent [12].

The feedback force F_1 and F_2 are defined as follows:

$$F_1{=}F_0 + \frac{ma}{2}, \tag{5.8}$$

$$F_2{=}F_0 - \frac{ma}{2}. \tag{5.9}$$

Following Equation (5.2), the force tracking errors are defined as follows:

$$\varepsilon_1(k+1) = F_{d1}(k) - F_1(k), \tag{5.10}$$

$$\varepsilon_2(k+1) = F_{d2}(k) - F_2(k). \tag{5.11}$$

The currents i_1 and i_2 with adaptive MNN controller are computed from Equation (5.1) and the corresponding network weights in (5.3) and (5.4), which are updated by the force tracking errors (5.10) and (5.11). Then the desired currents i_{d1} and i_{d2} are obtained as follows:

$$i_{d1} = i_1 + i_0, \tag{5.12}$$

$$i_{d2} = i_2 + i_0 \tag{5.13}$$

where the current i_0 corresponds to the bias force F_0 and can be determined experimentally.
The real net force $\hat{F}$ acting on the stage is the difference between the real forces $\hat{F}_1$ and $\hat{F}_2$:

$$\hat{F} = \hat{F}_1 - \hat{F}_2. \tag{5.14}$$

5.3 Simulations

Example 1: A simulation for the current-driven reluctance linear actuator is conducted to verify the performance of the proposed adaptive MNN control configuration shown in Figure 5.1. For comparison the nonlinear compensator Equation (3.1) is selected.

In this simulation, since the linear power amplifier has a high bandwidth and rapid response, it is ignored. For this reason, it is assumed that the I-target is fixed, so that we may investigate the force tracing performance. The reluctance linear actuator with hysteresis is modeled by Equation (2.80), whose parameters are chosen as in the patent [80] and shown in table (5.1).

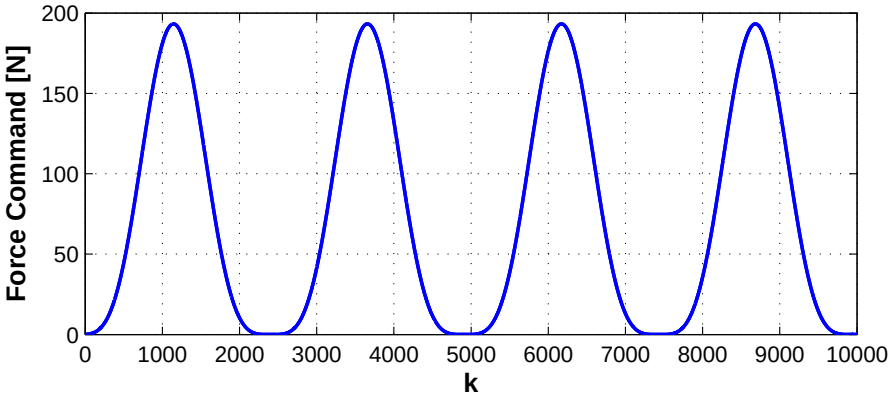

Figure 5.3: Force command.

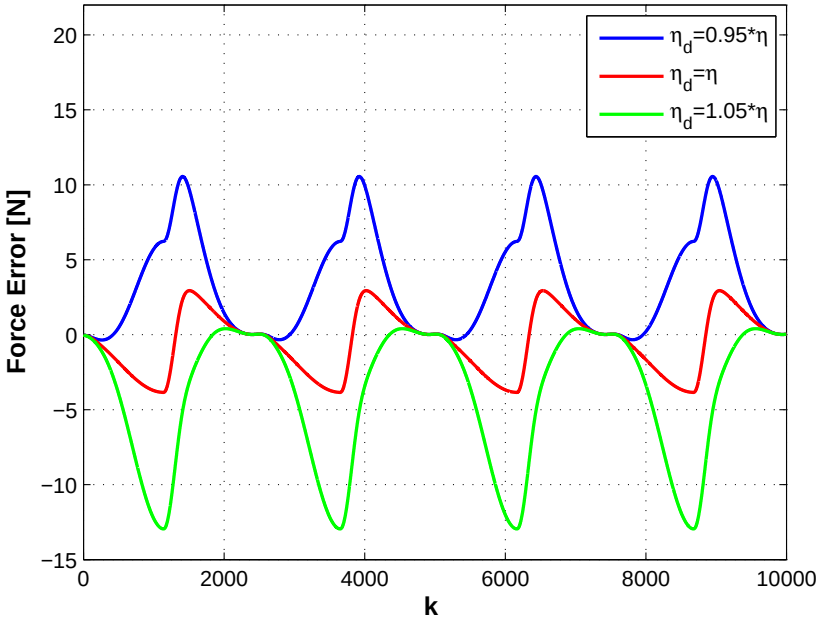

Figure 5.4: Force error with nonlinear compensator.

Items	Values
the maximum force	200 N
the maximum gap x_g	0.4 mm
the E/I constant	$k = 7.73 \times 10^{-6}$
the hysteresis operator parameters	$\lambda_1 = 0.02$ and $\lambda_2 = 10$

Table 5.1: E/I core parameters.

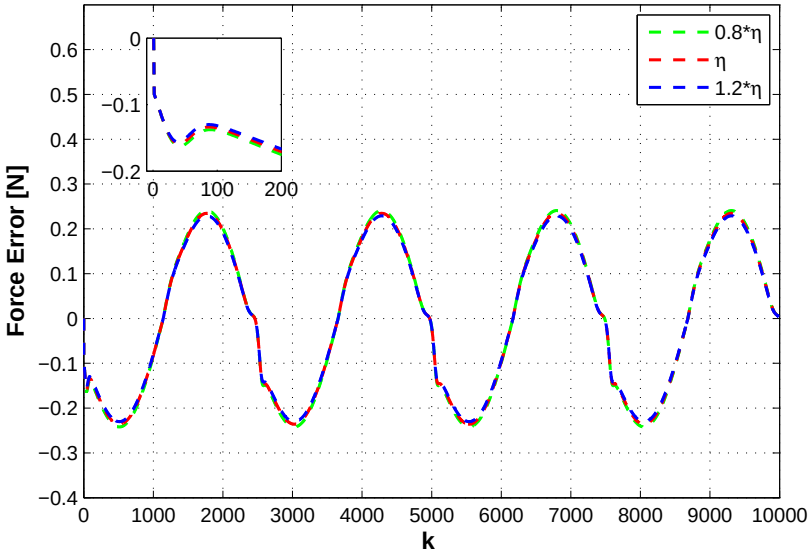

Figure 5.5: Force error with adaptive MNN controller.

The control objective is to make the system output F following the reference force F_d. The adaptive MNN controller Equation (5.1) is designed to reduce the influence of the nonlinearity including the hysteresis. Parameters of the adaptive MNN are determined as follows: the hidden-layer neurons are $l = 40$, the initialization neural network weighting matrices are $\mathbf{W}(0) = 0$ and $\mathbf{V}(0) = 0$. Equation (5.3) and Equation (5.4) are used to update the neural network weights, and the learning rate are selected as $\gamma_w = 0.00085$ and $\gamma_v = 0.01$.

The force tracking error between the input F_d and output F with nonlinear controller (3.1) is shown in Figure 5.4. When $\eta_d = \eta$, the force tracking error is about ± 4 N; when $\eta_d = 0.95\eta$, force tracking error is about from -12.5 N to 0.5 N; when $\eta_d = 1.05\eta$, force tracking error is about from -0.5 N to 11 N. It can

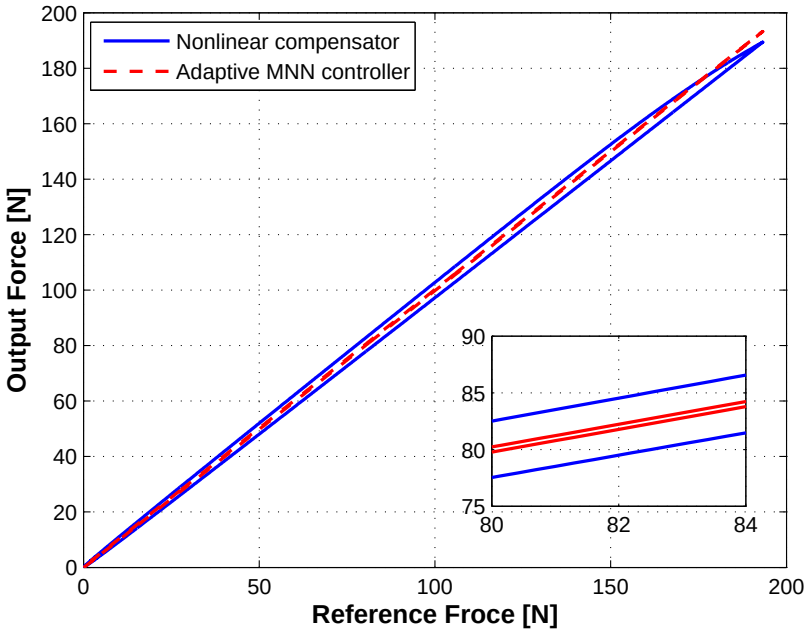

Figure 5.6: Comparison of the force hysteresis loop between nonlinear compensator and adaptive controller.

be seen that the force error increases with the error of η_d increases quickly. The force tracking error with adaptive MNN controller Equation 5.1 is shown in Figure 5.5. The force tracking error is about ± 0.25 N even if the E/I model parameter η varies up $\pm 20\%$. The reason is that the current command i_d is determined independent of the force model (2.66). Furthermore, Figure 5.6 shows that the ratio between the output force and its command is very close to 1 with adaptive controller. For comparison the nonlinear compensator (3.1) with parameter $\eta_d = \eta$ is selected. From the simulation results, it can be seen that the force with adaptive MNN control has a better tracking performance and robustness against parameter uncertainty than with nonlinear controller.

Example 2: In order to verify whether the proposed hysteresis compensation using adaptive MNN controller Equation (5.3) can be applied in high-precision systems, we do the following simulation on the one-degree-of-freedom stage as shown in Figure 5.3. Again, the nonlinear compensator (3.1) is used.

The gaps x_{g1} and x_{g2} between the E-core 1,2 and the stage are in the range of

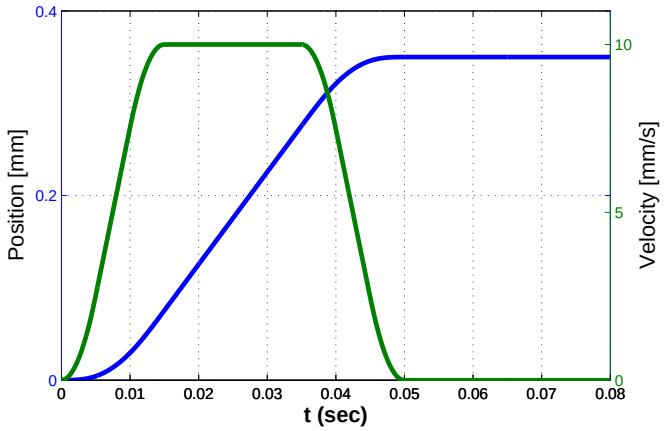

Figure 5.7: Reference position and velocity.

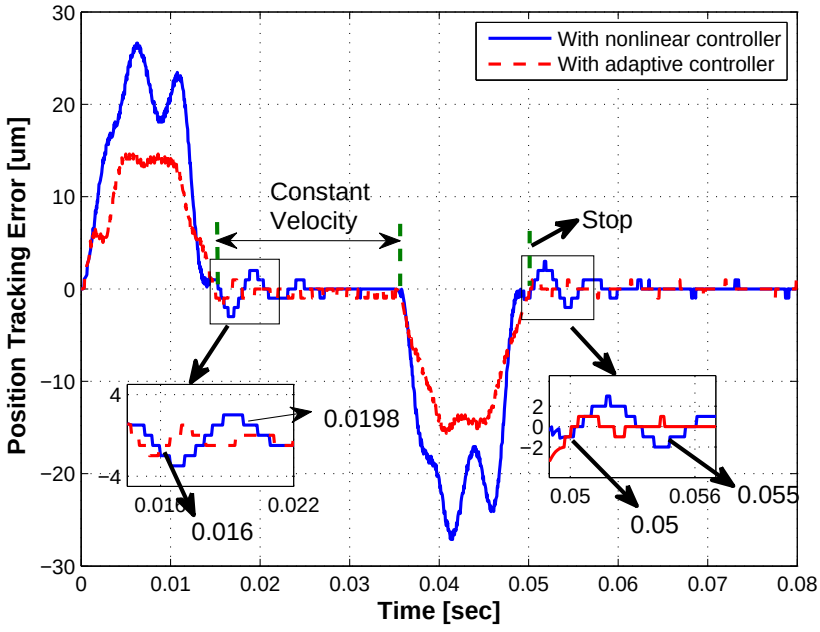

Figure 5.8: Comparison of the position tracking error between with nonlinear compensator and with adaptive MNN controller.

Items	Values
the stage mass	10 kg
the position sensor resolution	1 nm
the sampling time	$0.5ms$
the bias force	$F_0 = 15\ N$
The E-core electromagnetic constant	$k = 7.73 \times 10^{-6}$

Table 5.2: E/I stage simulation parameters.

0 μm to 400 μm and the initial gap is $x_{g0} = 400\ \mu m$. The E-core electromagnetic constant and parameters of hysteresis operator are set as in Example 1. The adaptive MNN parameters for the two E/I actuators are the same as in Example 1. The control objective is to make the stage position x follow the reference position. The reference trajectory is determined by the 3rd order trajectory planning method [43]. The position and velocity are shown in Figure 5.7. The trajectory values are shown in table (5.3).

Items	Values
the largest displacement	350 μm
the maximum velocity	10 mm/s
the maximum acceleration	1 m/s^2
the jerk	200 m/s^3

Table 5.3: Trajectory values.

The position tracking errors of control with nonlinear compensator (3.1) and with adaptive MNN controller (5.3) are shown in Figure 5.8. We define the constant velocity settling time and the stop time as the time instants after which the position tracking error is less than 1 μm. From the constant velocity segment, it can be seen that the constant velocity settling time with nonlinear compensator (0.0198 s) is about 1.22 times longer than of adaptive MNN controller (0.0162 s). From the stop segment, the stop time with nonlinear compensator (0.055 s) is about 1.1 times longer than that of adaptive MNN controller (0.05 s). The outputs of adaptive MNN controllers are shown in Figure 5.9 and the corresponding

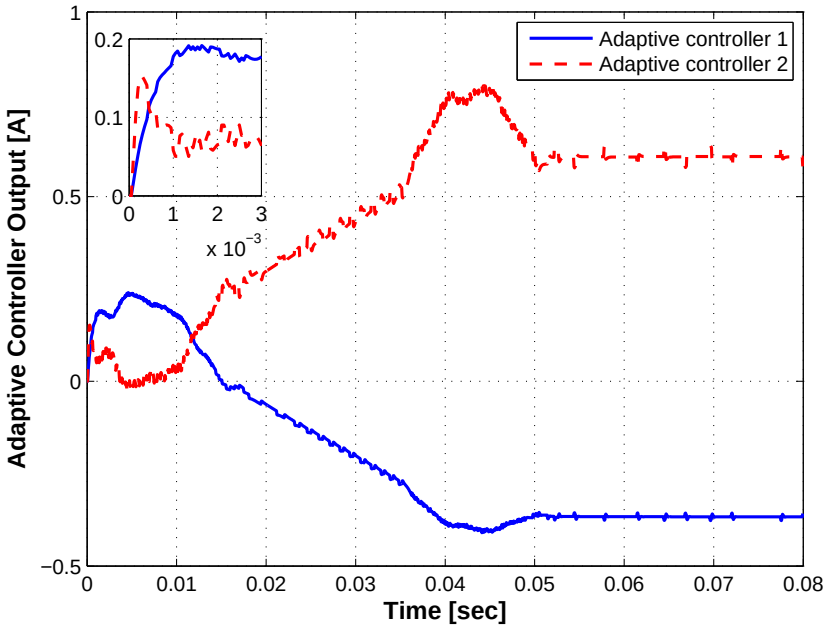

Figure 5.9: Outputs of the adaptive controllers.

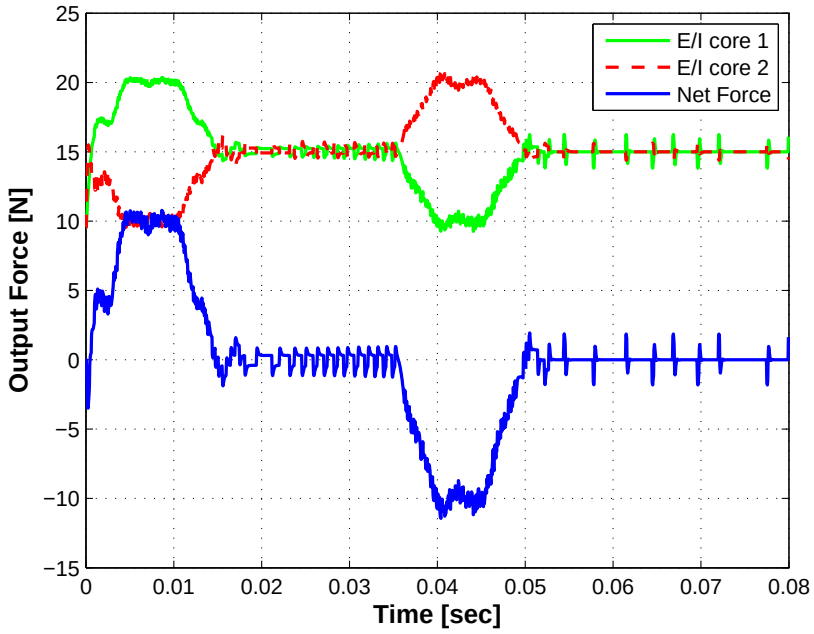

Figure 5.10: Output net force using the adaptive controller.

output force of the E/I core actuator 1, E/I core actuator 2 and difference in Figure 5.10.

5.4 Conclusion

This chapter has proposed a new direct adaptive MNN controller for the reluctance linear actuator with hysteresis. The direct adaptive MNN controller gets the desired current based on the desired force and actual force using an adaptive MNN, whose weights are updated using the projection function. Then the adaptive MNN controller is applied to a stage having paired E/I core actuator. Due to the simplicity of the nonlinear control configuration, it has a wider range of applications. The simulation results show that the proposed method is effective in over-coming the hysteresis parameter uncertainty and promising in high-precision control applications.

6

Acceleration Feedback in a Stage Having Paired Reluctance Linear Actuator with Hysteresis

6.1 Introduction

Conventionally, the positioning control design of a stage falls into two parts: (1) the actuator dynamics is omitted and the force is designed, (2) the current reference is computed from the designed force based on their static nonlinear relation [12]. But it does not consider the effect of hysteresis and parameter uncertainty on the force accuracy. For the hysteresis compensation, using the inverse hysteresis model [32] is the most noticeable. Reference [39] proposed an inverse hysteresis model and obtained a good performance for the reluctance linear actuator. However, these methods both need precise hysteresis model, which is generally complex and hardly to obtain. Owing to its online self-learning ability, the adaptive neural network can be used to hysteresis compensation methods proposed in **Chapter** 4 and **Chapter**g 5. However the neural network has a complex algorithm, so it cannot be easily applied in the real-time digital controller.

Acceleration feedback increases the mass of a system as experienced by disturbance force. Acceleration feedback has been applied to land gears [42] and the voice coil actuator [5] as an auxiliary to position control. The acceleration feedback complemented in an existing position controller for a wafer stage control has

been proposed in [10], which splits the acceleration controller into a forward and a backward path to create the original process behavior for position controller, and removes the high-bandwidth requirement.

In this paper, since the hysteresis influence on reluctance actuator is mainly in the low frequencies [38], by regarding the hysteresis force as a disturbance force, an acceleration feedback can be designed for the fine stage having paired reluctance linear actuator with hysteresis. The proposed method can improve the process sensitivity for low frequencies and remove the high-bandwidth requirement. Furthermore, acceleration feedback implementation in digital controller and control of the fine stage and coarse stage are discussed. The proposed method does not need the inverse hysteresis model and can be easily applied in the real time digital controller. Simulation results show that the proposed method is effective in overcoming the hysteresis force and promising in precision stage control.

6.2 Acceleration feedback control

6.2.1 Basic idea

Consider the relationship between the force command $F_d(d)$ and output force F in Figure 3.4, the hysteresis force error F_{hys} is defined as $F_{hys} = F_d - F$. Then from Figure 3.4, a simplified control scheme is shown in Figure 6.1, in which the stage transfer function $P_s(s)$ is simplified into two integrators and the fine stage mass m, ignoring extra dynamics in $P_s(s)$ and the other disturbance force. From Equation (3.3), if the mass of the fine stage is increased, while keeping the position control band width equal, we get the same output sensitivity but an improved process sensitivity. Since a larger mass is generally not expected for high acceleration control in the fine stage, increasing the virtual mass instead by the feedback of the acceleration in addition to the position, may improve the process sensitivity by reducing the influence of the force hysteresis.

6.2.2 Design of acceleration feedback in frequency domain

The idea of acceleration control introduced in [10] is reviewed below. A control structure using the acceleration feedback method as shown in Figure 6.2 is applied

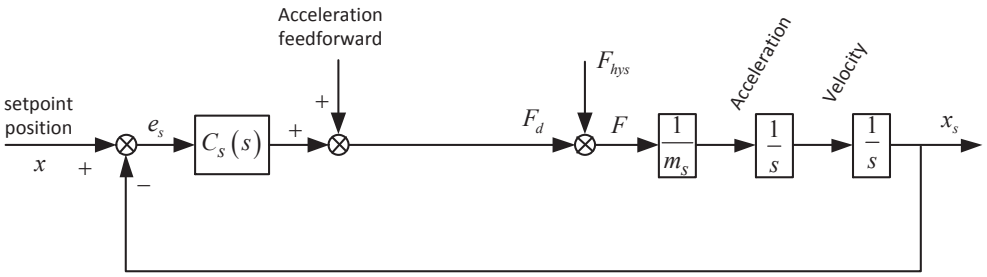

Figure 6.1: Simplified virtual control scheme.

to reduce the influence of the hysteresis in paired reluctance linear actuator. It is better that the position controller does not have any change in process behavior when the acceleration feedback loop is introduced. So the acceleration loop filter $H_1(s)$ and $H_2(2)$ are designed as such that the transfer function from the position controller output to stage acceleration remains the same, namely $1/m_s$:

$$\frac{H_1(s)/m_s}{1 + H_1(s)H_2(s)/m_s} = \frac{1}{m_s}. \tag{6.1}$$

From Equation (6.1), it follows that

$$H_1(s) = 1 + \frac{1}{m_s} H_a(s), \tag{6.2}$$

$$H_2(s) = \frac{H_a(s)}{1 + H_a(s)/m_s} \tag{6.3}$$

where $H_a(s) = H_1(s)H_2(s)$ and the hysteresis force rejection only depends on $H_a(s)$, which can be designed as a second-order lowpass filter or an integrator.

6.2.3 Acceleration feedback implementation for discretization

So far, the acceleration feedback used in paired reluctance actuator is considered in continuous-time domain. The sampling effects must be taken into account when the digital controller is applied in reality. Usually, there exits a delay of p

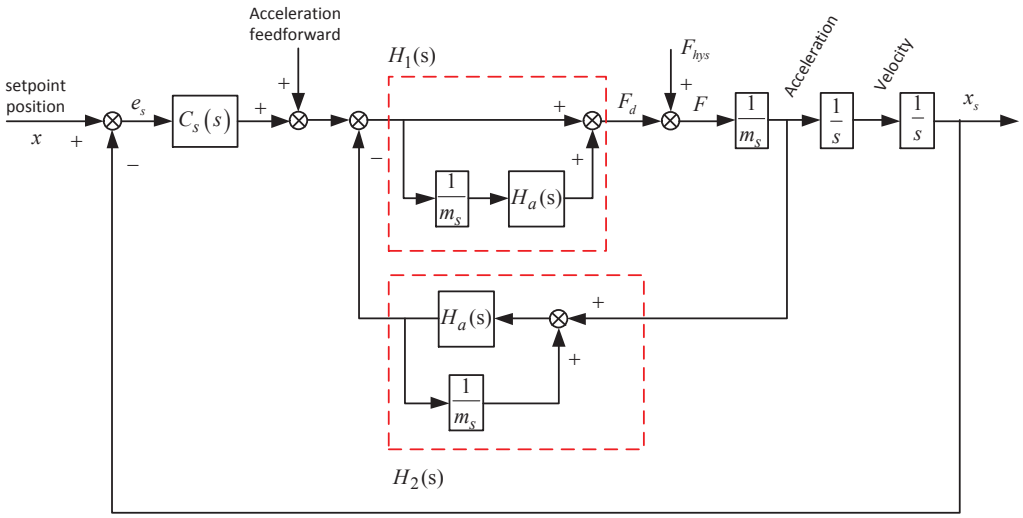

Figure 6.2: Using $H_1(s)$ and $H_2(s)$ in the acceleration feedback loop.

samples in the process transfer function and a delay of q samples caused by the acceleration measured. From Equation (6.1), we have:

$$\frac{\frac{z^{-p}}{m_s}H_1(z)}{1+\frac{z^{-(p+q)}}{m_s}H_1(z)H_2(z)} = \frac{z^{-p}}{m_s}. \tag{6.4}$$

The discrete acceleration feedback filter $H_1(z)$ and $H_2(z)$ corresponding to the delay p and q can be obtained as:

$$H_1(z) = 1 + \frac{z^{-(p+q)}}{m_s}H_a(z), \tag{6.5}$$

$$H_2(z) = \frac{H_a(z)}{1+\frac{z^{-(p+q)}}{m_s}H_a(z)}. \tag{6.6}$$

In reality the feedback acceleration a_m is calculated from the measured position x_s by a digital double differentiator as well

$$a_m = T(z)x_s = \frac{(1-z^{-1})^2}{T_s^2}x_s, \tag{6.7}$$

where T_s is the sampling period. A disadvantage of double differentiation is a possible introduction of noise. Since the closed acceleration loop has a lowpass

characteristic, it can reduce the noise. In addition, the least-squared method function used as filter may also reduce the noise impact [9].

From Figure 6.2, an original discrete form of acceleration feedback is shown in Figure 6.3. However, the acceleration feedforward signal will pass the increased order system caused by the acceleration feedback instead of passing through $P_s(z)$. This results in an increased position settling error compared to the situation without acceleration feedback [10]. Instead of increasing the feedforward order to cope with the process dynamics for reducing the position settling error, we shift the feedforward entry point towards the force command input into the acceleration feedback loop as shown in Figure 6.4. However, the feedforward force now enters the system loop at the same point as the hysteresis force. To avoid this problem, a relative acceleration is used by the deviation between the acceleration feedforward and the acceleration feedback [10]. A delay of $p + q$ samples must be used to match the acceleration feedback delay from the acceleration feedforward, and define $M(z) = \frac{z^{-(p+q)}}{m_s}$.

6.2.4 Acceleration feedback in a fine stage connected to a coarse stage

The practical reluctance linear actuator has a moving rang of only about $1mm$, which is insufficient for the stage in the lithographic equipment. This problem is solved by introducing a coarse stage actuated by the linear motor [8], which can travel over large distances with moderate micrometer-rang accuracy, and moves the fine stage actuated by the reluctance linear actuator [12]. Usually the E/I core part is connected to the coarse stage to avoid crossover of cables and cooling hoses to the accurate fine stage.

Based on Figure 6.3, a totally basic control scheme which combines the fine stage and coarse stage controllers with acceleration feedback loop is shown in Figure 6.5. Since the fine stage has a key roll in the final position accuracy, the acceleration feedback is added into the fine stage control loop. In Figure 6.5, $P_l(z)$ represents the coarse stage process system. The coarse stage is required to track the fine stage to keep the E/I core and fine stage close together. To this end, the gap sensors measure the gap distance between the coarse stage and fine

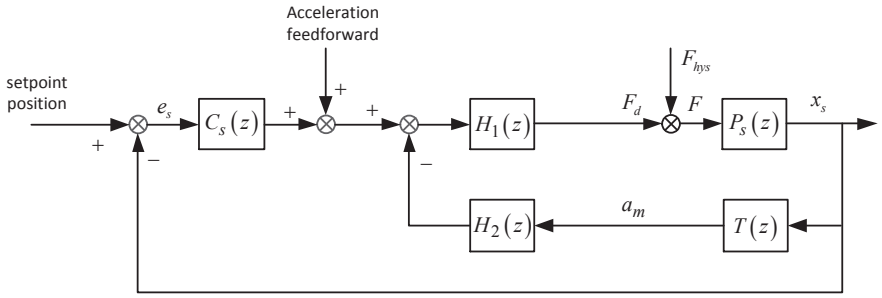

Figure 6.3: Discrete form of acceleration feedback.

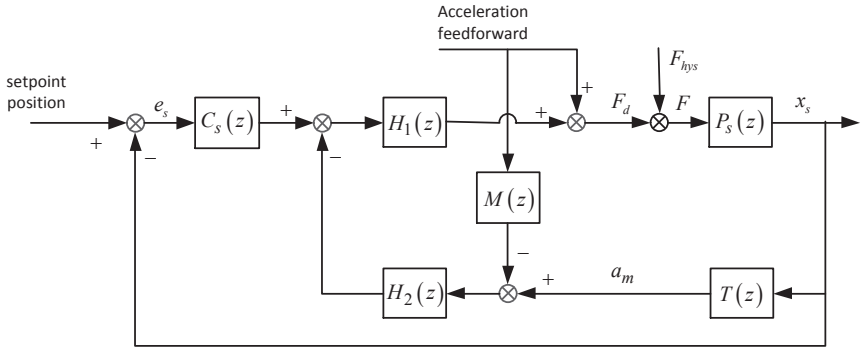

Figure 6.4: The final discrete form of acceleration feedback.

stage by the "gd"signal. As the fine stage is decoupled from the coarse stage by tracking the interferometer, the coarse stage controller $C_l(z)$ is designed for the dynamics of the coarse stage without taking the fine stage into account. In the feedforward path, since a reaction force is added to the coarse stage while the fine stage accelerates, the mass of the fine stage must be included to accelerate the coarse stage.

6.3 Simulations

In order to verify whether the proposed acceleration feedback configuration can be applied in high-precision systems, we do the following simulations on the scheme as shown in Figure 6.5. For comparison, the no acceleration feedback case is used.

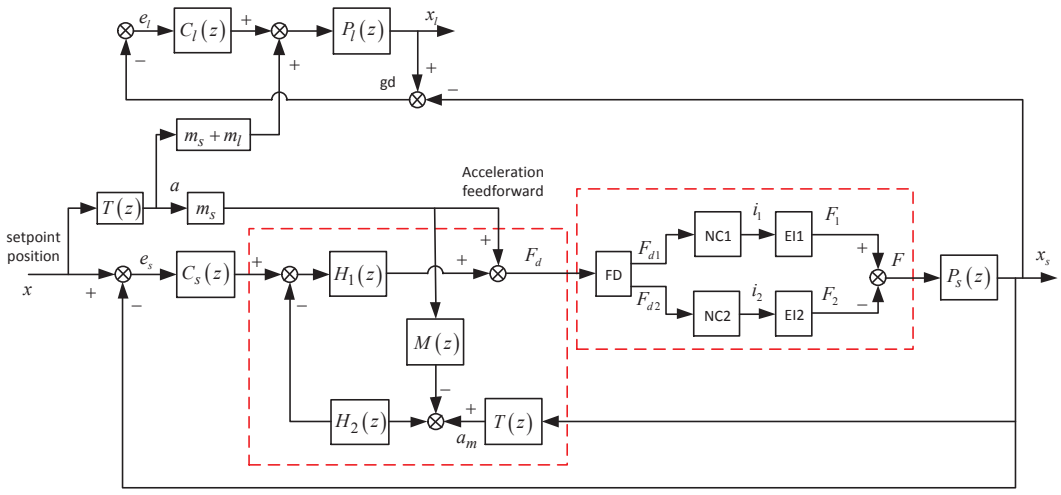

Figure 6.5: Total feedback scheme for coarse stage and fine stage using acceleration feedback.

The reluctance linear actuator with hysteresis is modeled by Equation (2.80), whose parameters are chosen as in the patent [80] and shown in table (6.1).

Items	Values
the maximum force	200 N
the maximum gap x_g	0.4 mm
the E/I constant	$k = 7.73 \times 10^{-6}$
the hysteresis operator parameters	$\lambda_1 = 0.02$ and $\lambda_2 = 10$

Table 6.1: E/I core parameters.

The gaps x_{g1} and x_{g2} between the E-core 1,2 and the stage are in the range of 0 μm to 400 μm and the initial gap is $x_{g0} = 400$ μm. The stage parameters are shown in table (6.2).

A typical setpoint position profile [8], which is used during exposing in lithographic equipment, is determined by the 3rd order trajectory planning method [43]. The position and velocity are shown in Figure 6.6, the scanning velocity settling time is defined as the time instants after which the position tracking error is less than 10 nm . The scanning velocity is 0.25 m/s, the acceleration is

Items	Values
the fine stage mass	10 kg
the coarse stage mass	20 kg
the position sensor resolution	1 nm
the sampling time	$0.5ms$
the bias force	$F_0 = 15\ N$
The E-core electromagnetic constant	$k = 7.73 \times 10^{-6}$

Table 6.2: E/I stage simulation parameters.

10 m/s^2.

In the practical application, the position controller is designed as a PI+lead compensator, which makes the position-controlled fine stage system having about a 100 Hz bandwidth corresponding the mechanical structure. The acceleration feedback filters $H_1(z)$ and $H_2(z)$ are designed as follows. $H_z(z)$ is chosen as an integrator with a gain that creates a closed acceleration loop bandwidth of $f_{abw} = 130Hz$, leading to

$$H_a(z) = \frac{2\pi m_s f_{abw} Ts}{1 - z^{-1}}. \tag{6.8}$$

By assuming that the process delay is $p = 1$ and the acceleration measurement delay is $q = 1$, then $M(z) = z^{-2}/m_s$. From Equation (6.5) and Equation (6.6), it follows that

$$H_1(z) = 1 + \frac{2\pi f_{abw} Ts}{1 - z^{-1}} z^{-2}, \tag{6.9}$$

$$H_2(z) = \frac{2\pi m_s f_{abw} Ts}{1 - z^{-1} + 2\pi f_{abw} Ts z^{-2}}. \tag{6.10}$$

The control objective is to make the stage position x_s follow the reference position x and have a quick scanning velocity settling time. Figure 6.7 shows the position tracking errors with and without acceleration feedback. The scanning velocity settling time is about 56 ms without acceleration feedback slower than with acceleration feedback 46 ms.

Figure 6.8 shows the fine stage position loop process sensitivity. we define the transfer function following Equation (3.3), which is added to the real force F as shown in Figure 6.5. From Figure 6.8, the fine stage position loop process

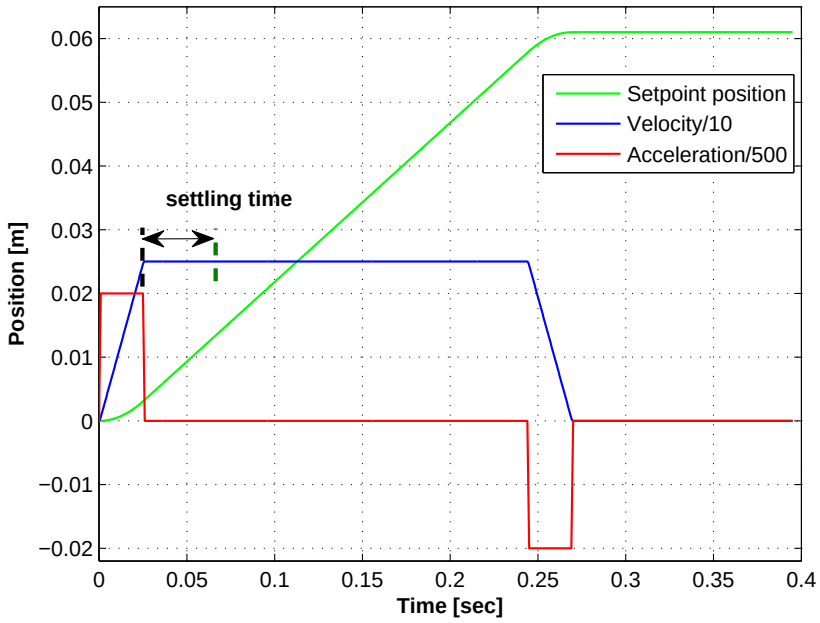

Figure 6.6: Reference position and velocity.

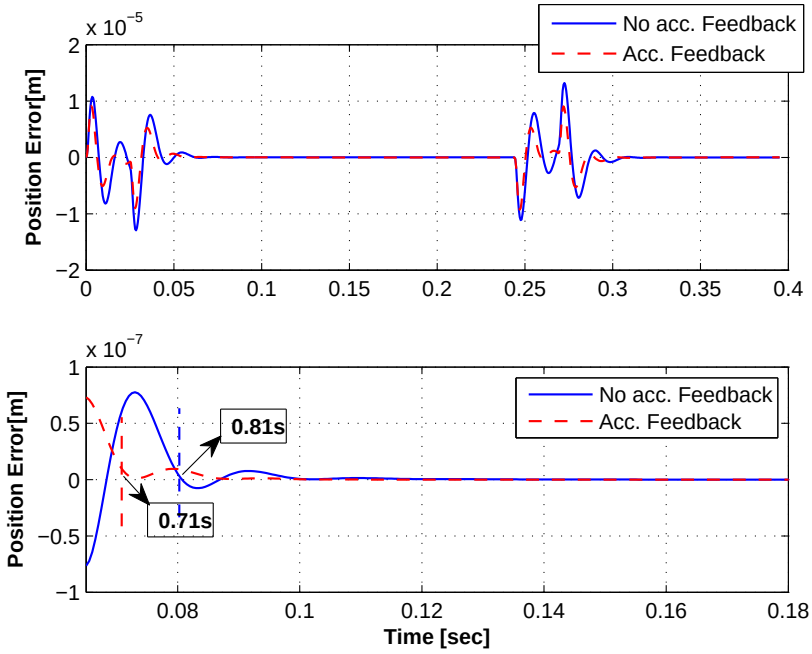

Figure 6.7: Position tracking error.

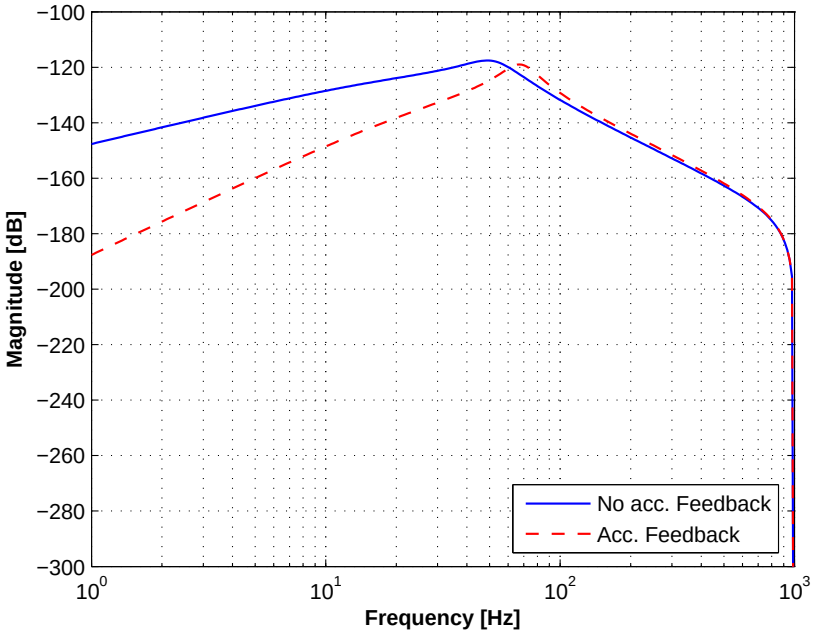

Figure 6.8: Position loop process sensitivity of the fine stage.

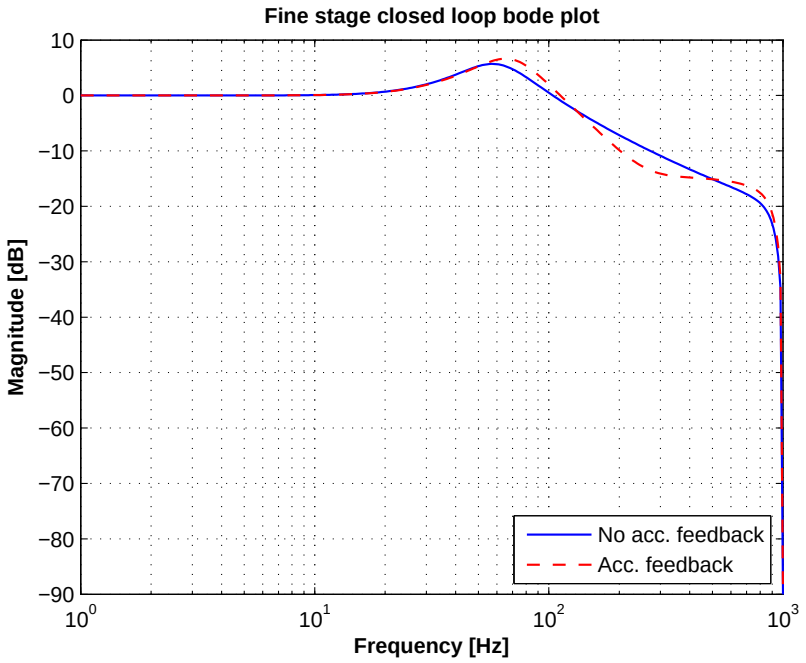

Figure 6.9: Fine stage closed control loop bode plots.

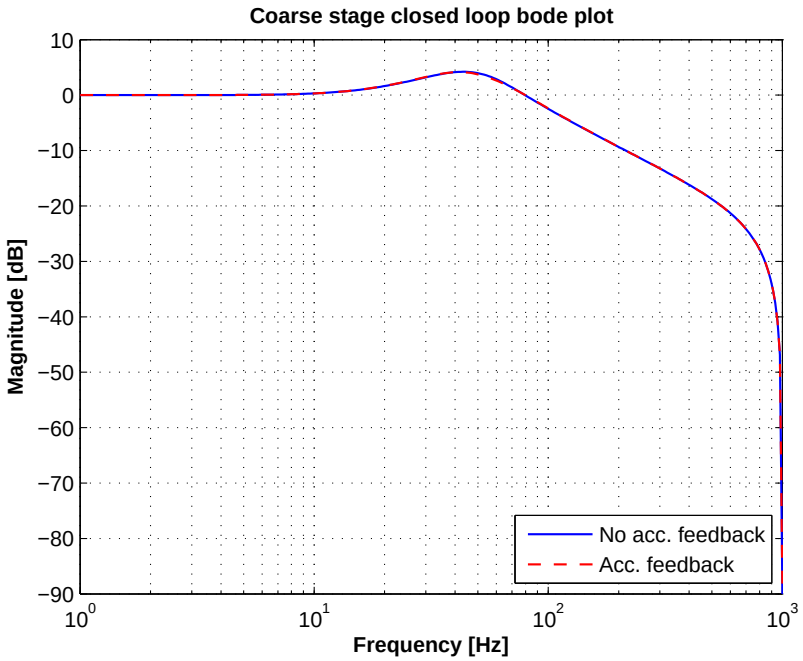

Figure 6.10: Coarse stage closed control loop bode plots.

sensitivity without acceleration feedback is about $-170\ dB$ and with acceleration feedback decreases to about $-230\ dB$ for low frequencies. It is clear that, the acceleration feedback introduced into the system provides a low process sensitivity for the hysteresis force.

The closed control loop bode plots of the fine stage with and without acceleration feedback are shown in Figure 6.9. It can be seen that, the acceleration feedback loop added into the system loop does not change the fine stage close loop for low frequencies, the magnitude increases a little at high frequencies. And closed control loop bode plots of the coarse stage with and without acceleration feedback is shown in Figure 6.10.

6.4 Comparison of the proposed hysteresis compensation methods

In the following, the comparison for the performance of the proposed hysteresis compensation methods in **Chapter** 4 -6 will be discussed by the simulations.

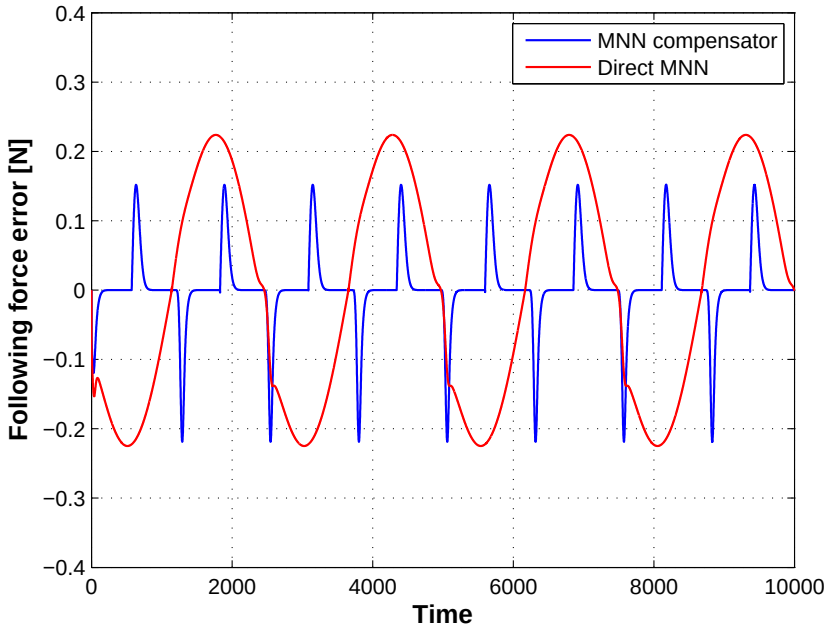

Figure 6.11: Comparison of the force following error.

Example 1: A simulation for the current-driven reluctance linear actuator is conducted to verify the performance of the proposed adaptive MNN compensator shown in Figure 4.1 in Chapter 4. For comparison the direct adaptive MNN shown in Figure 5.1 in Chapter 5. In this simulation, the reluctance actuator parameters and the adaptive MNN compensator parameters are selected as in Chapter 4 simulation Example 1. The parameters for the direct adaptive MNN compensation method proposed in Chapter 5 are selected as in Chapter 5 simulation example 1. The control objective is to make the system output F following the reference force F_d. A reference force depicted in Figure 5.3.

The comparison of the following force errors with adaptive MNN compensator proposed in Chapter 4 and direct adaptive MNN proposed in Chapter 5 is shown in Figure 6.11. We can find that the following force error with adaptive MNN compensator proposed in Chapter 4 has a smaller following force error and a quicker convergence time than the direct adaptive MNN proposed in Chapter 5. The main reason for difference of the following force error is that the nonlinear compensator is used in Chapter 4. *Example 2*: In order to verify the performance

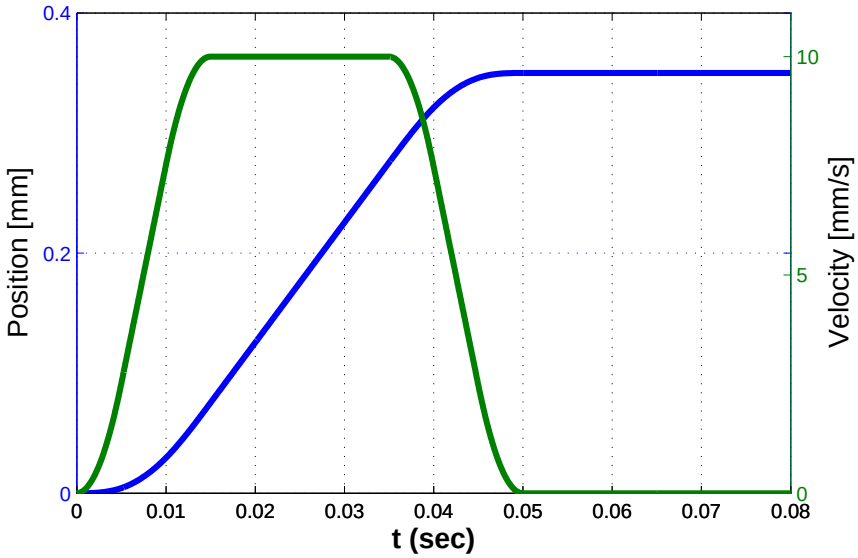

Figure 6.12: Reference position and velocity.

for the proposed methods in Chapter 4 - 6, do the simulations on the stage having the paired E/I core actuators. The parameters for the stage are selected as in Chapter 4 Example 2. The position and velocity values are chosen as in Chapter 4 Example 2 and trajectory is shown in Figure 6.12. The position following errors are shown in Figure 6.13. The adaptive MNN compensator proposed in Chapter 4, the direct adaptive MNN controller proposed in Chapter 5 and the the acceleration feedback method proposed in Chapter 6 have the same velocity settling time and stop time, but the acceleration feedback method proposed in Chapter 6 has a smaller following position error in the acceleration segment and deceleration segment.

Simulation results show that the proposed methods are effective in overcoming the hysteresis and promising in high-precision and high acceleration control applications. And the acceleration feedback method has better respects for the application. How to implement the proposed methods in the digital controller is the main next work.

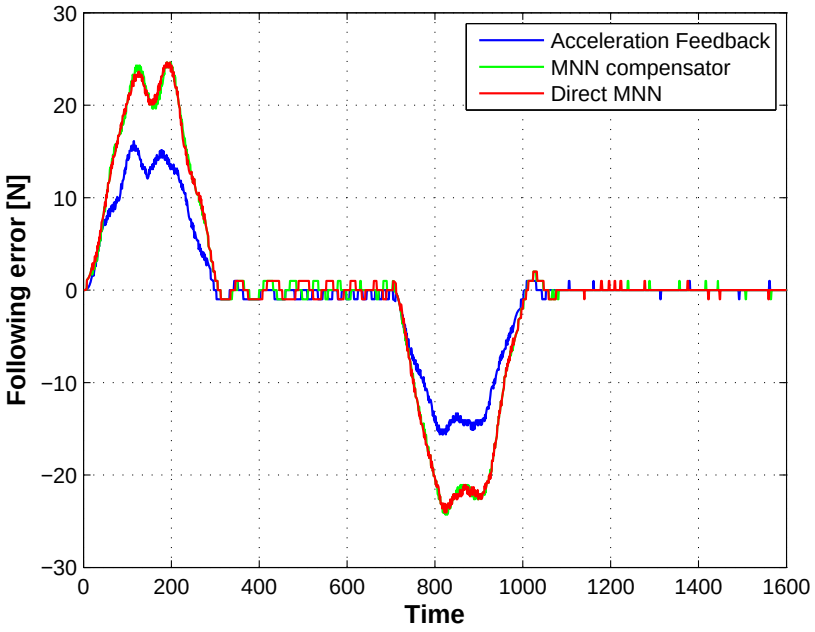

Figure 6.13: Comparison of the position tracking error.

6.5 Conclusion

This chapter has proposed a new acceleration feedback control method for the fine stage having paired reluctance linear actuator with hysteresis. By considering the fine stage force error caused by the hysteresis in the reluctance linear actuator, as a disturbance force and since the main hysteresis influence is in the low frequencies, the acceleration feedback loop can be design. The practical implementation has been discussed for the digital controller. The simulation results show that by properly choosing H_1 and H_2, the acceleration feedback can provide a low process sensitivity and a fast scanning velocity settling time. The proposed method is effective in overcoming the reluctance linear actuator with hysteresis and promising in high-precision control applications.

7

Conclusions

In this thesis, we introduce the thesis background, the challenge to the next-generation fine stage actuator and the main contributions in **Chapter** 1. In order to study the reluctance actuator, the models without hysteresis for the C-core and E-Core reluctance actuators are reviewed and the models with hysteresis for the C-core and E-Core reluctance actuators are proposed in **Chapter** 2. The reluctance models and the basic control method that introduced in **Chapter** 3 are the basic for this thesis works.

The main existing compensation methods for the reluctance actuator with hysteresis usually uses the inverse hysteresis models, which is complex and not easily to be implement. Owing to the online self-learning and estimation capability of the neural network, a hysteresis current compensation configuration for the reluctance actuator with hysteresis based on the adaptive multi-layer neural network is proposed in **Chapter** 4. The main contributions of this method is a hysteresis compensator for current-driven reluctance linear actuator using the adaptive MNN proposed for the first time and the inverse hysteresis model is not used.

Although the compensation method proposed in **Chapter** 4 may reduce the influence caused by the hysteresis on the reluctance force, the reluctance model is also used. A new nonlinear control method is proposed for the stage having paired reluctance linear actuator with hysteresis using the direct adaptive neural network is proposed in **Chapter** 5. The main advantage of the proposed adaptive MNN

controller is that the reluctance linear actuator model and the inverse hysteresis model are not required.

The compensation methods proposed in **Chapter** 4 and **Chapter** 5 are both used the adaptive MNN, but the complex structure and algorithm are difficultly implemented in the digital controller now. The acceleration feedback for the fine stage having paired reluctance linear actuator with hysteresis is designed in **Chapter** 6. The feature of this method lies in that by considering the hysteresis force as a disturbance force to design the acceleration feedback loop to reduce the influence of the hysteresis force. The proposed method can improve the process sensitivity for low frequencies and remove the high-bandwidth requirement. This acceleration feedback method could easily implemented in the digital controller.

Simulation results show that the proposed methods are effective in overcoming the hysteresis and promising in high-precision and high acceleration control applications. And the acceleration feedback method has better respects for the application. How to implement the proposed methods in the digital controller is the main next work.

References

[1] M. Al Janaideh, Feng Ying, S. Rakheja, Su Chun-Yi, and C. A. Rabbath. Hysteresis compensation for smart actuators using inverse generalized prandtl-ishlinskii model. In *American Control Conference, 2009. ACC '09.*, pages 307–312, 2009. 43

[2] J. S. Albus. A new approach to manipulator control: the cerebellar model articulation controller (cmac). *Journal of Dynamic Systems*, pages 220–227, 1975. 44

[3] A. Alessandri and T. Parisini. Nonlinear modeling of complex large-scale plants using neural networks and stochastic approximation. *IEEE Transactions on Systems, Man and Cybernetics, Part A: Systems and Humans*, 27(6):750–757, 1997. 45

[4] B Appelbe. Rate independent hysteresis in terrestrial hydrology. *IEEE Control Systems*, 29(1):44–69, 2009. 16

[5] A. Babinski and Tsao Tsu-Chin. Acceleration feedback design for voice coil actuated direct drive. In *American Control Conference, 1999. Proceedings of the 1999*, volume 5, pages 3713–3717 vol.5, 1999. 69

[6] Giorgio Bertotti. *Hysteresis in magnetism: for physicists, materials scientists, and engineers*. Academic press, 1998. 11, 19

[7] H. Butler. Scanning stage technology for exposure tools. *Microlithogr*, 8(2):8–16, 1999. 4

[8] H. Butler. Position control in lithographic equipment. *IEEE Control Systems*, 31(5):28–47, 2011. 2, 3, 5, 6, 7, 8, 38, 73, 75

[9] H. Butler. Adaptive feedforward for a wafer stage in a lithographic tool. *IEEE Transactions on Control Systems Technology*, PP(99):1–7, 2012. 47, 73

[10] Hans Butler. Acceleration feedback in a lithographic tool. *Control Engineering Practice*, 20(4):453–464, 2012. 70, 73

[11] A. Cavallo, C. Natale, S. Pirozzi, and C. Visone. Effects of hysteresis compensation in feedback control systems. *IEEE Transactions on Magnetics*, 39(3):1389–1392, 2003. 11

[12] Ping-Wei Chang. E/i core actuator commutation formula and control method, 2007. 40, 50, 51, 60, 69, 73

[13] V. Cherkassky, D. Gehring, and F. Mulier. Comparison of adaptive methods for function estimation from samples. *IEEE Transactions on Neural Networks*, 7(4):969–984, 1996. 44, 45

[14] R. M. Corless, G. H. Gonnet, D. E. G. Hare, D. J. Jeffrey, and D. E. Knuth. On the lambertw function. *Advances in Computational Mathematics*, 5(1):329–359, 1996. 17

[15] G. Cybenko. Approximation by superpositions of a sigmoidal function. *Mathematics of Control, Signals and Systems*, 2(4):303–314, 1989. 44

[16] A. M. Dabroom and H. K. Khalil. Output feedback sampled-data control of nonlinear systems using high-gain observers. *IEEE Transactions on Automatic Control*, 46(11):1712–1725, 2001. 45

[17] Avinash Dixit. Hysteresis, import penetration, and exchange rate pass-through. *The Quarterly Journal of Economics*, pages 205–228, 1989. 16

[18] A. A. Eielsen, J. T. Gravdahl, and K. Y. Pettersen. Adaptive feedforward hysteresis compensation for piezoelectric actuators. *Rev Sci Instrum*, 83(8):085001, 2012. 11

[19] James Alfred Ewing. On the production of transient electric currents in iron and steel conductors by twisting them when magnetised or by magnetising them when twisted. *Proceedings of the Royal Society of London*, 33(216-219):21–23, 1881. 15

[20] Lin Faa-Jeng, Shieh Hsin-Jang, and Huang Po-Kai. Adaptive wavelet neural network control with hysteresis estimation for piezo-positioning mechanism. *IEEE Transactions on Neural Networks*, 17(2):432–444, 2006. 43, 57

[21] Chen Fu-Chuang and H. K. Khalil. Adaptive control of a class of nonlinear discrete-time systems using neural networks. *IEEE Transactions on Automatic Control*, 40(5):791–801, 1995. 44

[22] Kenchi Funahashi. On the approximate realization of continuous mappings by neural networks. *Neural Networks*, 2(3):183–192, 1989. 44, 45

[23] William S Galinaitis and Robert C Rogers. Control of a hysteretic actuator using inverse hysteresis compensation. In *5th Annual International Symposium on Smart Structures and Materials*, pages 267–277. International Society for Optics and Photonics, 1998. 16

[24] S. S. Ge, C. C. Hang, and Zhang Tao. Adaptive neural network control of nonlinear systems by state and output feedback. *IEEE Transactions on Systems, Man, and Cybernetics, Part B: Cybernetics*, 29(6):818–828, 1999. 45

[25] S. S. Ge, C. C. Hang, and T. Zhang. Nonlinear adaptive control using neural networks and its application to cstr systems. *Journal of Process Control*, 9(4):313–323, 1999. 45

[26] S S Ge, Chang C Hang, Tong H Lee, and Tao Zhang. *Stable adaptive neural network control*. Springer Publishing Company, Incorporated, 2010. 57, 58

[27] S. S. Ge and C. Wang. Adaptive control of uncertain chua's circuits. *IEEE Transactions on Circuits and Systems I: Fundamental Theory and Applications*, 47(9):1397–1402, 2000. 45

[28] C. J. Goh. Model reference control of non-linear systems via implicit function emulation. *Int. J. Control*, 60(90-115), 1994. 44

[29] J. Q. Gong and Yao Bin. Adaptive robust control without knowing bounds of parameter variations. In *Decision and Control, 1999. Proceedings of the 38th IEEE Conference on*, volume 4, pages 3334–3339 vol.4, 1999. 48

[30] William B Haines. Studies in the physical properties of soil. v. the hysteresis effect in capillary properties, and the modes of moisture distribution associated therewith. *The Journal of Agricultural Science*, 20(01):97–116, 1930. 15

[31] Kurt Hornik, Maxwell Stinchcombe, and Halbert White. Multilayer feedforward networks are universal approximators. *Neural Networks*, 2(5):359–366, 1989. 44

[32] R. V. Iyer and Tan Xiaobo. Control of hysteretic systems through inverse compensation. *IEEE Control Systems*, 29(1):83–99, 2009. 11, 43, 69

[33] R. V. Iyer and Tan Xiaobo. Control of hysteretic systems through inverse compensation. *IEEE Control Systems*, 29(1):83–99, 2009. 11

[34] Ram V Iyer and Matthew E Shirley. Hysteresis parameter identification with limited experimental data. *IEEE Transactions on Magnetics*, 40(5):3227–3239, 2004. 16

[35] L. Jin, P. N. Nikiforuk, and M. M. Gupta. Direct adaptive output tracking control using multilayered neural networks. *IEEE Proceedings Control Theory and Applications*, 140(6):393–398, 1993. 44

[36] Oh Jinhyoung, B. Drincic, and D. S. Bernstein. Nonlinear feedback models of hysteresis. *IEEE Control Systems*, 29(1):100–119, 2009. 43

[37] Oh Jinhyoung, B. Drincic, and Bernstein D S. Nonlinear feedback models of hysteresis. *IEEE Control Systems*, 29(1):100–119, 2009. 16

[38] A. Katalenic, J. de Boeij, H. Butler, and P. P. J. van den Bosch. Linearization of a current-driven reluctance actuator with hysteresis compensation. *Mechatronics*, 23(2), 2013. 11, 70

[39] Boeij J. Katalenic A. Linearization of the reluctance force actuator based on the parametric hysteresis inverse and a 2d spline. In *Proceedings of the 8th International Symposium on Linear Drives for Industry Applications (LDIA 2011)*, 2011. 16, 19, 41, 43, 69

[40] Pavel Krejci and Vladimir Lovicar. Continuity of hysteresis operators in sobolev spaces. *Aplikace matematiky*, 35(1):60–66, 1990. 16

[41] Klaus Kuhnen. Modeling, identification and compensation of complex hysteretic nonlinearities: A modified prandtl ishlinskii approach. *European Journal of Control*, 9(4):407–418, 2003. 16

[42] Seung-Keon Kwak, Gregory Washington, and Rama K Yedavalli. Acceleration feedback-based active and passive vibration control of landing gear components. *Journal of Aerospace Engineering*, 15(1):1–9, 2002. 69

[43] Paul Lambrechts, Matthijs Boerlage, and Maarten Steinbuch. Trajectory planning and feedforward design for electromechanical motion systems. *Control Engineering Practice*, 13(2):145–157, 2005. 52, 66, 75

[44] K. K. Leang and S. Devasia. Iterative feedforward compensation of hysteresis in piezo positioners. In *Proceedings. 42nd IEEE Conference on Decision and Control, 2003*, volume 3, pages 2626–2631 Vol.3, 2003. 16

[45] K K Leang, Zou Qingze, and S. Devasia. Feedforward control of piezoactuators in atomic force microscope systems. *IEEE Control Systems*, 29(1):70–82, 2009. 16

[46] A. U. Levin and K. S. Narendra. Control of nonlinear dynamical systems using neural networks. ii. observability, identification, and control. *IEEE Transactions on Neural Networks*, 7(1):30–42, 1996. 44

[47] Yu-Ping Liu, Kang-Zhi Liu, and Xiaofeng Yang. A direct adaptive mnn control method for stage having paired reluctance linear actuator with hysteresis. *Intelligent Control and Automation*, 5(04):213, 2014. 12, 57

[48] Yu-Ping Liu, Kang-Zhi Liu, and Xiaofeng Yang. Nonlinear current control for reluctance actuator with hysteresis compensation. *Journal of Control Science and Engineering*, 4, 2014. 12

[49] Yuping Liu, Lianfei ZHAI, and Tianyou Chai. Nonlinear adaptive pid control using neural networks and multiple models and its application. *Journal of Chemical Industry and Engineering (China)*, 7:013, 2008. 43, 44, 57

[50] Erwin Madelung. Uber magnetisierung durch schnellverlaufende strome und die wirkungsweise des rutherford marconischen magnetdetektors. *Annalen der Physik*, 322(10):861–890, 1905. 15

[51] I. Mayergoyz. *Mathematical Models of Hysteresis*. New York: SpringerVerlag, 1991. 16

[52] John C. McCallum. Historical cost of computer memory and storage, 2013. 8, 9

[53] Chen Min and C. R. Knospe. Feedback linearization of active magnetic bearings: current-mode implementation. *IEEE/ASME Transactions on Mechatronics*, 10(6):632–639, 2005. 11

[54] S. Mittal and C. H. Menq. Hysteresis compensation in electromagnetic actuators through preisach model inversion. *IEEE/ASME Transactions on Mechatronics*, 5(4):394–409, 2000. 11

[55] S. Mittal and C. H. Menq. Hysteresis compensation in electromagnetic actuators through preisach model inversion. *IEEE/ASME Transactions on Mechatronics*, 5(4):394–409, 2000. 43

[56] G. E. Moore. Cramming more components onto integrated circuits. *Electron. Mag.*, 38(8):4–7, 1965. 9

[57] P. E. Moraal and J. W. Grizzle. Observer design for nonlinear systems with discrete-time measurements. *IEEE Transactions on Automatic Control*, 40(3):395–404, 1995. 45

[58] van Eijk J. Munnig Schmidt S., Schitter G. *The design of high performance mechatronics*. Delft University Press, Netherlands, 2011. 1, 2, 4

[59] K. S. Narendra and S. Mukhopadhyay. Adaptive control of nonlinear multivariable systems using neural networks. In *Proceedings of the 32nd IEEE Conference on Decision and Control, 1993*, volume 4, pages 3066–3071, 1993. 44

[60] K. S. Narendra and K. Parthasarathy. Identification and control of dynamical systems using neural networks. *IEEE Transactions on Neural Networks*, 1(1):4–27, 1990. 44

[61] San Phyo Phyo, Ren Beibei, S. S. Ge, Lee Tong-Heng, and Liu Jin-Kun. Adaptive neural network control of hard disk drives with hysteresis friction nonlinearity. *IEEE Transactions on Control Systems Technology*, 19(2):351–358, 2011. 43, 57

[62] W. S. McCulloch Pitts and W. A logical calculus of the ideas immanent in nervous activity. *Bull. Math. biophys*, 5:115–133, 1943. 44, 45

[63] M. Krasnoselskii Pokrovskii and A. *M. Krasnoselskii and A. Pokrovskii*. New York: Springer-Verlag, 1989. 16

[64] M. M. Polycarpou and P. A. Ioannou. Learning and convergence analysis of neural-type structured networks. *IEEE Transactions on Neural Networks*, 3(1):39–50, 1992. 44

[65] F. Preisach. Uber die magnetische nachwirkung. *Zeitschrift fur Physik*, 94(5-6):277–302, 1935. 15

[66] ASML Products. Pas 5500/100d, i-line stepper, 2014. 3

[67] ASML Products. Pas 5500/1150c, 193-nm step-and-scan, 2014. 5

[68] ASML Products. Twinscan nxe:3300b, 2014. 6, 7

[69] D. Psaltis, A. Sideris, and A. A. Yamamura. A multilayered neural network controller. *IEEE Control Systems Magazine*, 8(2):17–21, 1988. 44

[70] D E Rumelhart. Learning internal representations by error propagation. *Parallel Distributed Processing*, 1(362-378), 1986. 44

[71] N. Sadegh. A perceptron network for functional identification and control of nonlinear systems. *IEEE Transactions on Neural Networks*, 4(6):982–988, 1993. 44, 45

[72] Andre M. Shaw and Francis J. Doyle Iii. Multivariable nonlinear control applications for a high purity distillation column using a recurrent dynamic neuron model. *Journal of Process Control*, 7(4):255–268, 1997. 45

[73] Ralph C Smith. *Smart material systems: model development*, volume 32. Siam, 2005. 16

[74] G. Song, Zhao Jinqiang, Zhou Xiaoqin, and J. A. De Abreu-Garcia. Tracking control of a piezoceramic actuator with hysteresis compensation using inverse preisach model. *IEEE/ASME Transactions on Mechatronics*, 10(2):198–209, 2005. 16

[75] M. Brokate Sprekels and J. *Hysteresis and Phase Transitions*. New York: Springer-Verlag, 1996. 16

[76] Fu-Chun Sun, Han-Xiong Li, and Lei Li. Robot discrete adaptive control based on dynamic inversion using dynamical neural networks. *Automatica*, 38(11):1977–1983, 2002. 45

[77] Xiaobo Tan and John S. Baras. Modeling and control of hysteresis in magnetostrictive actuators. *Automatica*, 40(9):1469–1480, 2004. 16

[78] Gang Tao and Petar V Kokotovic. *Adaptive control of systems with actuator and sensor nonlinearities*. John Wiley Sons, Inc., 1996. 16

[79] Intel technology news. Toshiba starts mass production of world's first 15nm nand flash memorie, 2014. 9

[80] Ting-Chien Teng and Bausan Yuan. Stage having paired e/i core actuator control, 2000. 38, 39, 61, 75

[81] A. T. Vemuri and M. M. Polycarpou. Neural-network-based robust fault diagnosis in robotic systems. *IEEE Transactions on Neural Networks*, 8(6):1410–1420, 1997. 45

[82] A. T. Vemuri, M. M. Polycarpou, and S. A. Diakourtis. Neural network based fault detection in robotic manipulators. *IEEE Transactions on Robotics and Automation*, 14(2):342–348, 1998. 45

[83] Augusto Visintin. *Differential models of hysteresis*, volume 1. Springer Berlin, 1994. 15

[84] J. W. Vrijsen, N. H. Jansen. Comparison of linear voice coil and reluctance actuators for high-precision applications. In *2010 14th International Power Electronics and Motion Control Conference (EPE/PEMC)*, pages S3–29–S3–36, 2010. 10

[85] C. Wang and S. S. Ge. Adaptive synchronization of uncertain chaotic systems via backstepping design. *Chaos, Solitons Fractals*, 12(7):1199–1206, 2001. 45

[86] Smith F W Widrow B. Pattern-recognizing control systems. *Computer and Information Sciences (COINS) Proceedings*, 1964. 44

[87] Qingsong Xu and Yangmin Li. Dahl model-based hysteresis compensation and precise positioning control of an xy parallel micromanipulator with piezoelectric actuation. *Journal of Dynamic Systems, Measurement, and Control*, 132(4):041011, 2010. 43

[88] X. Xue and J. Tang. Robust and high precision control using piezoelectric actuator circuit and integral continuous sliding mode control design. *Journal of Sound and Vibration*, 293(1-2):335–359, 2006. 11

[89] Liu Yu-Ping, Liu Kang-Zhi, and Yang Xiaofeng. Hysteresis compensation control for reluctance actuator force using neural network. In *2013 32nd Chinese Control Conference (CCC)*, pages 3354–3359, 2013. 57

[90] T. Zhang. Neural-based direct adaptive control for a class of general nonlinear systems. *International Journal of Systems Science*, 28(10):1011–1020, 1997. 45

List of Publications

International Journal Papers

- Yu-Ping Liu, Kang-Zhi Liu, and Xiaofeng Yang, (2014) Nonlinear Current Control for Reluctance Actuator with Hysteresis Compensation, *Journal of Control Science and Engineering*, vol. 2014.
- Liu, Y. P., Liu, K. Z., Yang, X. (2014). A Direct Adaptive MNN Control Method for Stage Having Paired Reluctance Linear Actuator with Hysteresis. *Intelligent Control and Automatio*n, 5(04), 213.

International Conference Papers

- Yu Ping Liu, kang Zhi Liu and Xiaofeng Yang, (2014) Hysteresis Compensation Control for a Current-driven Reluctance Actuator Using the Adaptive MNN. *Applied Mechanics and Materials*, 643, 60.
- Liu, Y. P., Liu, K. Z., Yang, X. (2013). Hysteresis compensation control for reluctance actuator force using neural network. *In Control Conference (CCC), 2013 32nd Chinese* (pp. 3354-3359).